10-24-2018

New Borehole Breakout Derived Stress Constraints and their Implications for Stress Heterogeneity Near High Risk Fault Systems in the Santa Barbara Channel, Southern California

Edward Harris Pritchard
Louisiana State University and Agricultural and Mechanical College

NEW BOREHOLE BREAKOUT DERIVED STRESS CONSTRAINTS AND THEIR IMPLICATIONS FOR STRESS HETEROGENEITY NEAR HIGH-RISK FAULT SYSTEMS IN THE SANTA BARBARA CHANNEL, SOUTHERN CALIFORNIA

A Thesis

Submitted to the Graduate Faculty of the
Louisiana State University and
Agricultural and Mechanical College
In partial fulfillment of the
requirements for the degree of
Master of Science

in

The Department of Geology and Geophysics

by
Edward Pritchard
B.S. Washington and Lee University, 2016
December 2018

ACKNOWLEDGEMENTS

First and foremost, I would like to thank Dr. Patricia Persaud for the massive amount of time and effort that she has put into serving as my thesis and graduate school advisor for the past two years. There have been many, many ups and downs, and without her patience and willingness to understand I never could have made it through. She has been an invaluable intellectual resource to me, and as her first student, we have both learned and grown throughout this process.

I would also like to thank the oil companies in the southern California area who provided the data for this project. In addition to providing the data, they have also answered any questions we have had regarding the data, helping this project run smoothly.

Thank you to Chris Sorlien, Marc Kamerling, Craig Nicholson, and Richard Behl for sharing their work. A special extra thanks to Chris Sorlien for going out of his way to compile the seismic profiles and fault surfaces, and for making himself available to questions.

Thank you to the Southern California Earthquake Center funding part of this work.

Thank you to my thesis committee members for keeping me on the right track, and providing me with sage advice.

Finally, thank you to my friends and family for their love, support, and belief in me. I would especially like to thank my parents for their unending support, Alison Coy for always being there for me, loving me, and picking me up when I am down, and Blake Odom, a life long friend, for being great company, and for allowing me to move into his home for the past several months.

TABLE OF CONTENTS

ABSTRACT

The Santa Barbara Channel represents the offshore portion of the Ventura Basin in Southern California. Ongoing transpression related to a regional left step in the San Andreas Fault has led to the formation of E-W trending en-echelon fault systems, with both north and south dips, which accommodate varying rates of localized shortening across the basin. Recent studies have suggested that faults within the northern region of the channel could be capable of a multisegment rupture and producing a M_w 7.7–8.1 tsunamigenic earthquake. However, dynamic rupture models producing these results have not accounted for stress heterogeneity, which is known to limit earthquake size. With limited information available on the stress field in the Santa Barbara Channel, new constraints on crustal stress could prove essential for obtaining a more comprehensive understanding of the hazards related to the complex fault systems in this region.

We use oriented 4-arm caliper data from 19 deviated wells obtained from industry to identify stress induced borehole breakouts beneath the Holly and Gail oil platforms in the Santa Barbara Channel. A misfit-based forward modeling technique is used to provide quantitative constraints on the orientations and relative magnitudes of the three principal stresses beneath each platform. At platform Gail, we determine a reverse faulting stress regime with S_{Hmax} trending N45°E (confidence range N40°E - N55°E). Our results are consistent with local structures, which reflect deeper regional scale trends, and with similar studies onshore nearby. At platform Holly, limited breakout azimuthal coverage in deviated wells restricted our ability to uniquely constrain the stress regime and S_{Hmax} orientation. However, our results indicate a reverse, oblique reverse, or strike-slip regime, and breakouts in near-vertical wellbore sections indicate mean S_{Hmax} orientations of N56.76°E ± 24.3° and N35.88°W ± 16.1° at different depths. Our results are partially consistent with the expected sense of slip along proximate fault systems, but differ from nearby onshore and offshore results, indicating stress heterogeneity in the north channel region. We conclude that borehole breakouts may record stress heterogeneity near active faults at the short length-scales (<10 km laterally and <1 km in depth) important for seismic hazard studies.

CHAPTER 1. INTRODUCTION

The Transverse Ranges province (Figure 1.1A), a major structural and geomorphic province in southern California, is characterized by its east-west trending anticlinal mountain ranges and synclinal basins, which transverse the dominant northwest structural grain of the rest of the state (Hadley and Kanamori, 1977; Vedder et al., 1969). The westernmost extent of this province is the Santa Barbara Channel (Figure 1.1B), which is an east-west trending tectonic depression that represents a submerged part of the Transverse Ranges, and the offshore westward continuation of the Ventura Basin (Vedder et al., 1969). Rapid tectonic convergence (~2.5 - 7 mm/yr) in the greater Ventura region (Marshall et al., 2013) has led to elevated background seismicity, several low magnitude (M0.0 - M2.8) earthquake swarms, and several moderate to large events including the 1812 M_w >7 earthquake, the 1925 M_w 6.3 and 1978 M_w 5.1 Santa Barbara earthquakes, the 1971 M_w 6.7 San Fernando earthquake, and the 1994 M6.7 Northridge earthquake, which was one of the most expensive natural disasters in the history of the United States (Hauksson et al., 2016; Marshall et al., 2013; Sorlien and Kamerling, 2000).

Repeated 6-8 m marine uplift terraces at Pitas Point, just west of Ventura, have been cited as evidence that damaging ~M_w 8.0 earthquakes have occurred in the western Transverse Ranges at a recurrence interval of 1-2 ka, with the last event occurring ~950 years ago (Rockwell et al., 2014). Hubbard et al. (2014) produced a fault representation of the onshore Ventura fault in which it is structurally linked at depth with the Pitas Point and San Cayetano faults, forming a single continuous fault surface of >100 km, which they believe may be capable of a massive, multisegment rupture, and producing a M_w 7.7-8.1 tsunamigenic earthquake. Dynamic rupture models based on the fault representations from Hubbard et al. (2014) have supported these claims (Ryan et al., 2015). However, the fault representations of Hubbard et al. (2014) were created by extrapolating onshore fault geometries 30 km into the offshore basin., and it has been noted that a more complete understanding of the complex offshore fault geometries and segment boundaries, as well as the nature of slip across them would be beneficial to any assessment of the probability of multi-segment earthquakes in this region (Sorlien and Nicholson, 2015).

Another key factor is the influence that stress field variations may have in fault rupture mechanics. Current dynamic rupture and ground motion models typically incorporate regional stress by applying a single, homogenous stress regime to entire fault systems (Barall and Harris, 2015). Studies have indicated, however, that the local stress field near earthquake faults is not homogenous (Rivera and Kanamori, 2002), and likely varies substantially, especially at geometric complexities such as step-overs or bends (Liu et al., 2016; Rivera and Kanamori, 2002). Furthermore, studies of model sensitivity to changes in stress inputs have indicated that increased stress heterogeneity tends to produce shorter rupture lengths (Lozos et al., 2015), and minor rotations to the orientation of maximum compressive stress (30°) can reduce calculated peak ground velocities by over 40% (Roten et al., 2014). Thus, dynamic rupture and ground motion models must take stress heterogeneity into account. Although only a few constraints on stress orientations beneath the Santa Barbara Channel exist, previous studies have indicated that they are not uniform throughout the region (Mount and Suppe, 1992; Wilde and Stock, 1997). If incorporated into future models, improved constraints on stress heterogeneity will allow for a more precise definition of initial stresses and will therefore contribute to more accurate predictions of rupture scenarios and their resulting ground motions.

As part of ongoing Southern California Earthquake Center (SCEC) Community Stress Model efforts to constrain and improve our understanding of 4D stress in the southern California lithosphere, we use borehole breakouts to present new constraints on the stress regimes beneath two offshore oil platforms in the Santa Barbara Channel. Our results, when combined with those of previous borehole breakout studies in the region, provide insight into the scale at which borehole breakouts record crustal stress, as well as the scale at which stress heterogeneity exists in the upper 1.8 km of crust beneath this region.

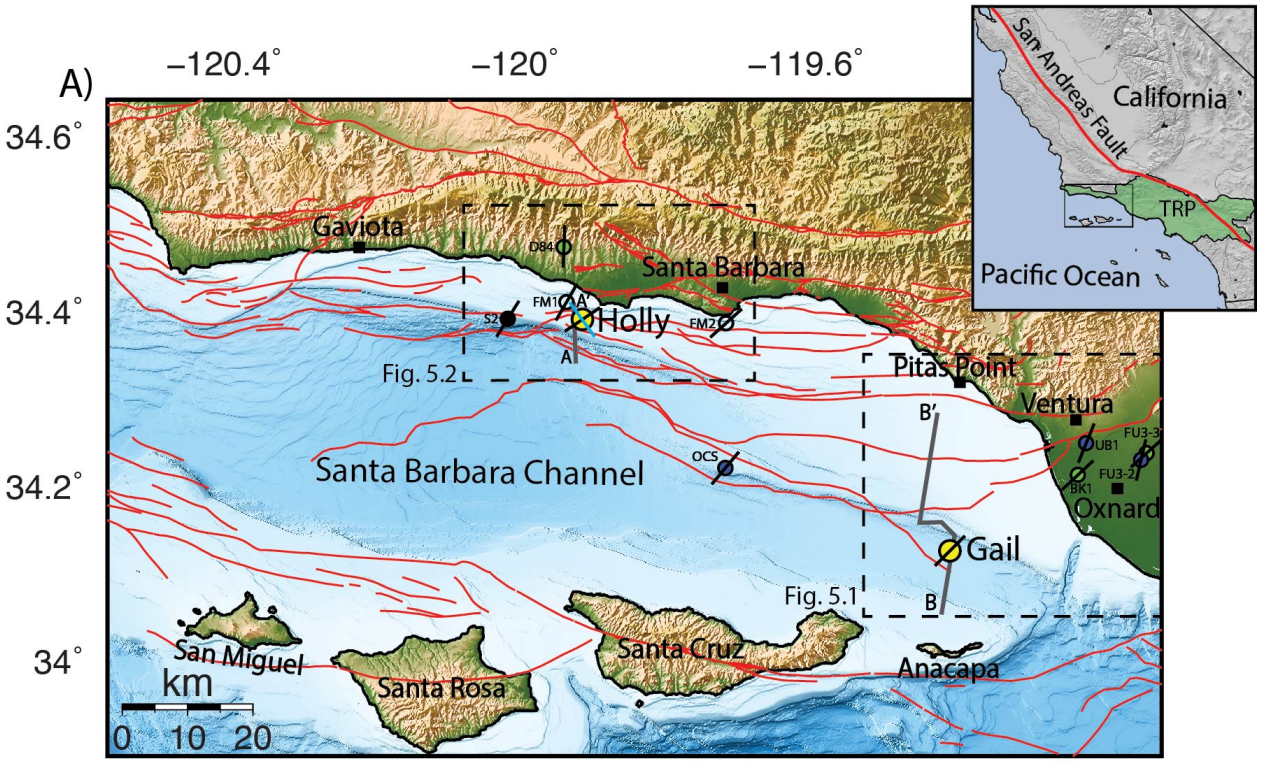

Figure 1.1 A) Map of the Santa Barbara Channel with bathymetry and topography. Yellow circles mark the locations of platforms Holly and Gail, a black circle marks the location of the well used by Heck and Edwards (1998), green circles show the Wilde and Stock (1997) wells, and blue circles show the Mount and Suppe (1992) wells. The locations of two WSM single earthquake focal mechanisms (FM1 & FM2) are shown with empty circles. S_{Hmax} orientations from each stress indicator are shown by black lines, and the blue line at platform Holly represents S_{Hmax} at 558 - 566 m TVD. Red lines onshore are the Quaternary faults from Jennings and Bryant (2010), offshore red lines are fault traces from Sorlien et al. (2016), black dashed boxes represent the extents of Figures 12 and 13, and grey lines represent the locations of the 2D seismic reflection lines A-A' and B-B'. Inset map shows our study area in the Santa Barbara Channel outlined with a black box. The Transverse Ranges Province (TRP) is shown with green shading and the San Andreas Fault with a red line. The digital elevation model was obtained from Divins, D.L., and D. Metzger, NGDC Coastal Relief Model, Retrieved date October 20, 2018 http://www.ngdc.noaa.gov/mgg/coastal/coastal.html. B) Map of the Santa Barbara Channel including regional fault surfaces (Nicholson, 2017; Sorlien et al., 2016). Platform Holly is located in the north channel region near a structurally complex zone of the Pitas Point (PPF) - North Channel (NCF) - Red Mountain (RMF) faults systems. Platform Gail is located in the eastern end of the mid-channel region in a less structurally complex zone near the Western Deep, Mid-Channel, and Oak Ridge Faults. White dashed boxes represent the extents of Figures 2.1A and 2.3A.
(Figure Continued.)

B)

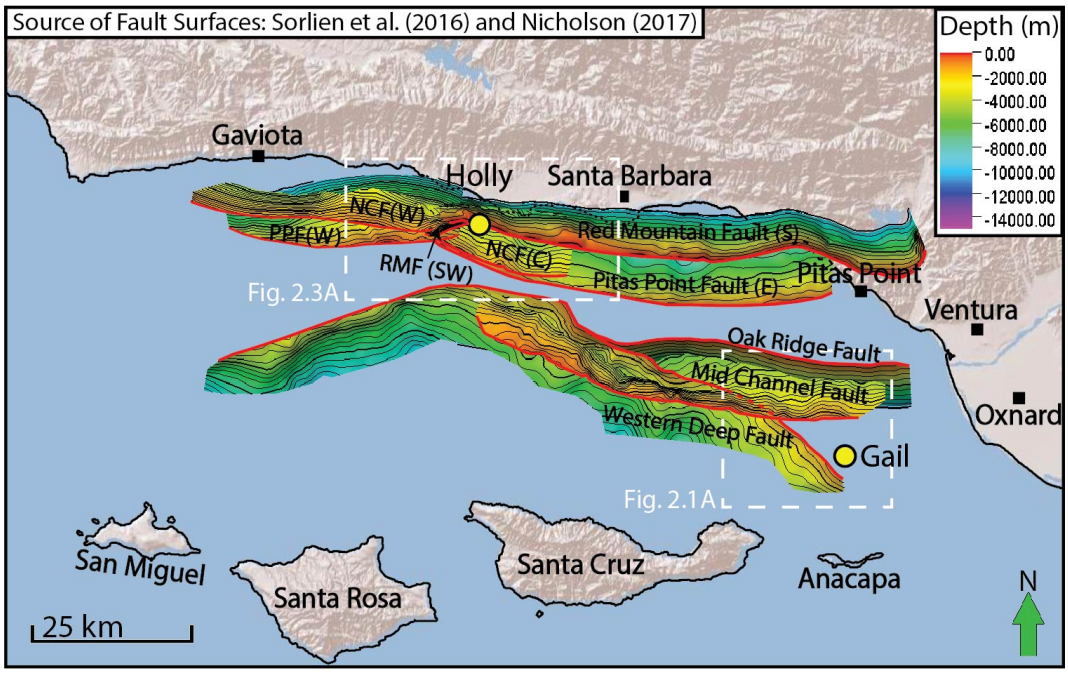
Source of Fault Surfaces: Sorlien et al. (2016) and Nicholson (2017)
Depth (m)
0.00
-2000.00
-4000.00
-6000.00
-8000.00
-10000.00
-12000.00
-14000.00
Gaviota
Holly
Santa Barbara
NCF(W)
PPF(W)
RMF (SW)
NCF(C)
Red Mountain Fault (S)
Pitas Point Fault (E)
Pitas Point
Ventura
Fig. 2.3A
Oak Ridge Fault
Mid Channel Fault
Western Deep Fault
Gail
Oxnard
Fig. 2.1A
San Miguel
Santa Rosa
Santa Cruz
Anacapa
25 km
N

CHAPTER 2. BACKGROUND

2.1. Geological setting of the Santa Barbara Channel

The Santa Barbara Channel exists in its present form as a result of Miocene extension followed by recent and ongoing transpression (Atwater, 1970; Atwater and Stock, 1998; Crouch and Suppe, 1993; Dickinson, 1996; Ingle, 1980; Kamerling and Luyendyk, 1985; Marshall, 2012; Nicholson et al., 1994; Seeber and Sorlien, 2000). The extensional regime began during the late Oligocene to early Miocene when the Farallon plate began subducting beneath the North American Plate, and capture of the Monterey microplate caused as much as 90-100° clockwise rotation of the Western Transverse Ranges Province (Atwater and Stock, 1998; Atwater, 1989; Marshall, 2012; Nicholson et al., 1994). This rotation led to oblique rifting which formed the Santa Barbara - Ventura Basin (Atwater and Stock, 1998; Kamerling and Luyendyk, 1985; Marshall, 2012). Roughly 12-13 Ma, capture of the Guadalupe and Magdalena microplates initiated early extension within the Gulf of California, which rotated Baja California ~10° clockwise (Nicholson et al., 1994). This rotation, combined with a change in geometry and an eastward jump of the Pacific-North America plate boundary into the Gulf of California, initiated a more transpressional regime across southern California, and produced a collision across a regional scale left step in the San Andreas Fault called the Mojave Restraining Segment (Figure 1.1A) (Ingle, 1980; Larsen et al., 1993; Larson and Webb, 1992; Marshall, 2012; Pinter et al., 1998).

The modern structural complexity of the Santa Barbara Channel stems from this collision at the Mojave Restraining Segment, which led to ongoing NNE-SSW shortening across the entire Western Transverse Ranges Province. Regionally, this contraction led to rapid uplift of the Transverse Ranges, and rapid subsidence of the synclinal Santa Barbara-Ventura Basin (Ingle, 1980; Larsen et al., 1993; Larson and Webb, 1992; Marshall, 2012; Pinter et al., 1998). Within the Santa Barbara Channel itself, normal and/or strike-slip faults that developed during Miocene extension were reactivated within an actively contracting fold-thrust belt (Shaw and Suppe, 1994; Sibson, 2004; Yeats et al., 1988). Currently, various rates of shortening across the basin are accommodated by several east-west trending en-echelon fault systems, with both north and south dips, which transverse the north and mid-channel regions, and control an overlying series of tight, asymmetric, anticlinal folds (Figure 1.1B) (Nicholson, 2017; Sorlien and Nicholson, 2015; Sorlien et al., 2016).

2.2. Structural setting of platforms Gail and Holly

Platform Gail of our dataset is located at approximately 34° 7'N; 119° 24’ W (Figure 1.1A,B) and targets the Sockeye Oil Field in the southeastern region of the Santa Barbara Channel roughly 15 km northeast of Santa Cruz Island and 20 km southeast of Oxnard, California. The platform sits just north of the S-dipping, NW-striking Western Deep Fault, and south of the N-dipping, E-W striking Mid Channel Fault, which intersects at depth with the steeply S-dipping E-W striking Oak Ridge Fault to the north (Figure 2.1A) (Nicholson, 2017; Sorlien et al., 2016). Of these faults, both the Western Deep and Mid-Channel faults are blind, with sea floor deformation expressed as extensive folding rather than fault offset (Figure 2.2) (Sorlien et al., 2016). On a more local scale, however, the shallow structure beneath platform Gail seems to be most consistent with that of the NW-striking Western Deep Fault. Wells from the platform target the Sockeye Anticline structure, which is a broad, NW-trending, doubly plunging

anticline bound both to the north and southwest by S-dipping, NW-striking thrust faults (Figure 2.1B) (DOGGR, 1992; Sankur et al., 1990).

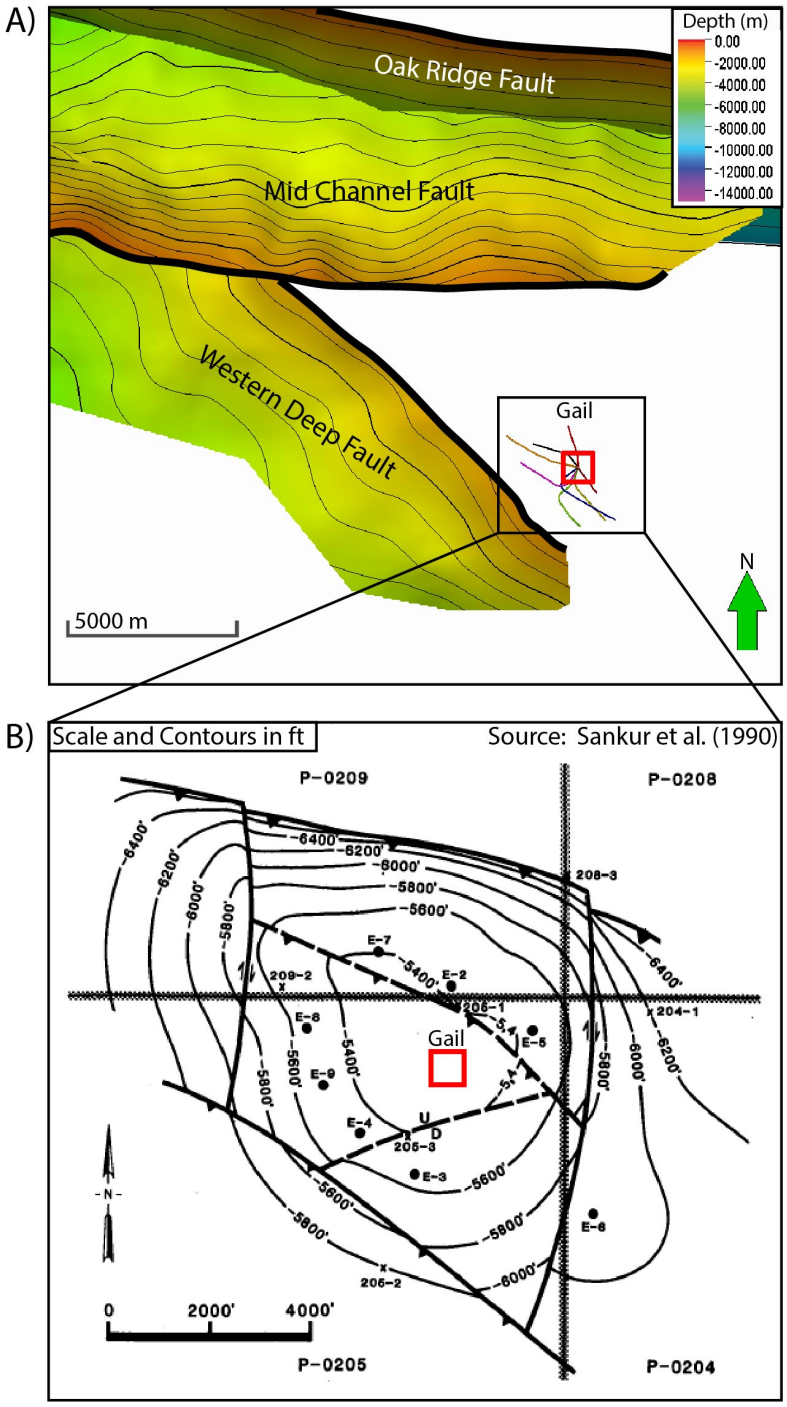

Figure 2.1 A) View of platform Gail well paths from directly overhead showing the proximity of the platform to the NW-striking Western Deep Fault and the Mid-Channel fault, which intersects the Oak Ridge fault at depth to the north. B) Contour map of Sockeye Sespe Unconformity (Sankur et al., 1990) showing the NW-trending Sockeye Anticline structure, which is cut by NW-striking thrust faults that extend from at least 1.5 - 2 km depth towards the surface (Sankur et al., 1990).

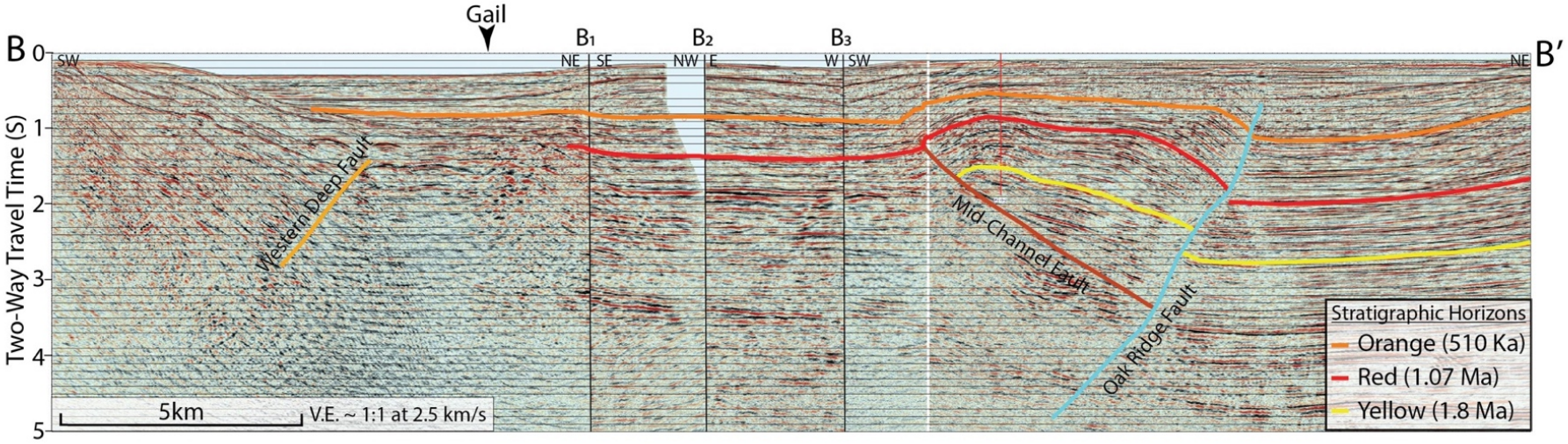

Figure 2.2 Composite 2D seismic reflection profile with both stratigraphic (Behl et al., 2016) and fault interpretations (Sorlien and Nicholson, 2015). The profile runs roughly NE-SW with an ~5 km left step from B_1 to B_3 (see Figures 1.1A, 5.1 for profile location). Segment B - B_1 is 240 m west of platform Gail, and shows the proximity of the platform to the S-dipping Western Deep fault. To the north of platform Gail, the N-dipping Mid-Channel fault intersects the Oak Ridge fault at depth.

Platform Holly of our dataset is located at approximately 34° 23'N; 119° 54' W (Figure 1.1A,B), and targets the South Ellwood Oil Field located roughly 8 km west of the University of California, Santa Barbara (UCSB) in the structurally complex northern region of the Santa Barbara Channel. This region is dominated by the N-dipping faults of the Pitas Point - North Channel - Red Mountain fault systems, segments of which extend 120 km west from Ventura (Figure 1.1B). The two deepest faults of this system, the Pitas Point and North Channel faults, are blind faults with surface deformation expressed as folding rather than fault offset (Figure 2.4) (Sorlien and Nicholson, 2015). These two faults extend nearly the entire length of the channel, with few changes to their generally E-W orientation. However, both faults experience brief, but significant changes in orientation near the location of platform Holly, where there is a segment boundary in the North Channel Fault, and a 25° continuous right-stepping double-bend in the Pitas Point Fault (Figure 2.3A,B) (Sorlien and Nicholson, 2015). Both of these faults briefly strike NW-SE in this small area, and then return to an E-W orientation as they extend westward. In this same location, there is also a change in strike of the much shallower Red Mountain Fault, which offsets the sea floor in many locations (Figure 2.4). Near platform Holly, the Red Mountain Fault is split into two segments. The Red Mountain (S) segment, located mostly east of Holly strikes E-W, but the Red Mountain (SW) segment located west of Holly, briefly strikes NE-SW before merging with the underlying blind faults to the west (Figure 2.3A) (Sorlien and Nicholson, 2015).

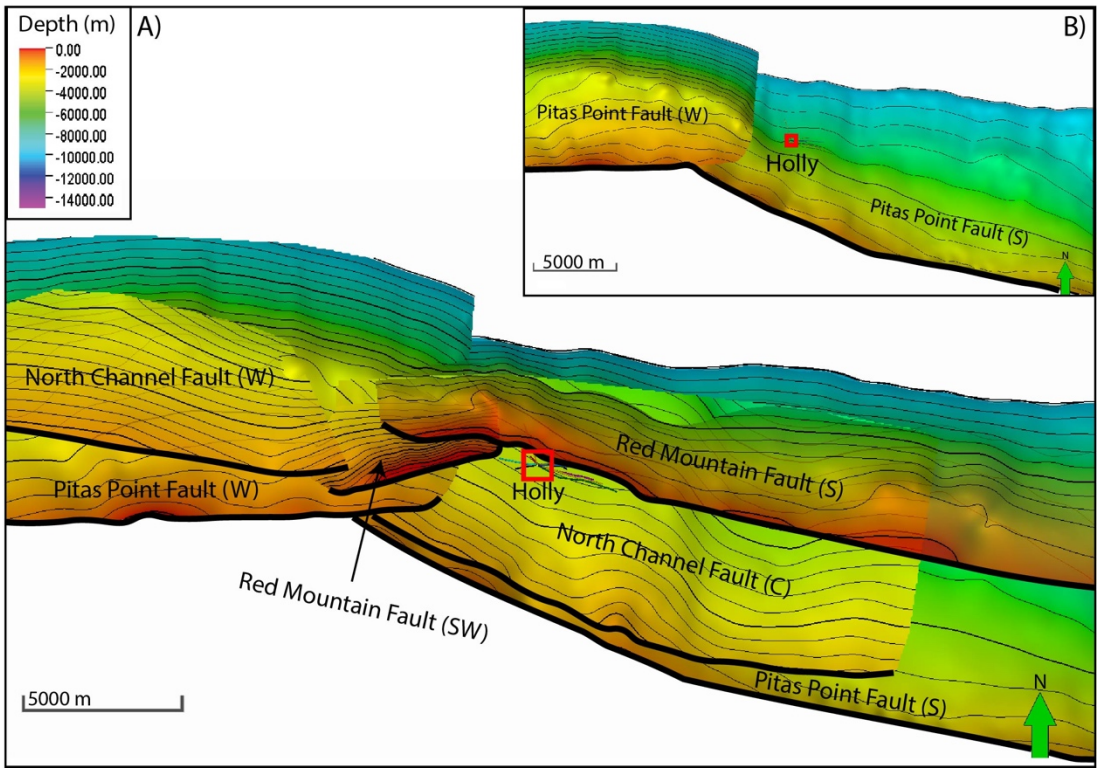

Figure 2.3 A) View of platform Holly well paths from directly overhead showing the proximity of the platform to a structurally complex zone where the Pitas Point, North Channel, and Red Mountain faults all exhibit major changes in orientation. The platform is located nearest to the Red Mountain (S) and Red Mountain (SW) fault segments. The Red Mountain (SW) segment differs in orientation from the general E-W or NW-SE structural trend of the region. B) View of platform Holly and the Pitas Point fault, which underlies segments of the North Channel and Red Mountain faults, and strikes NW-SE beneath the platform due to a roughly 25° bend in its strike.

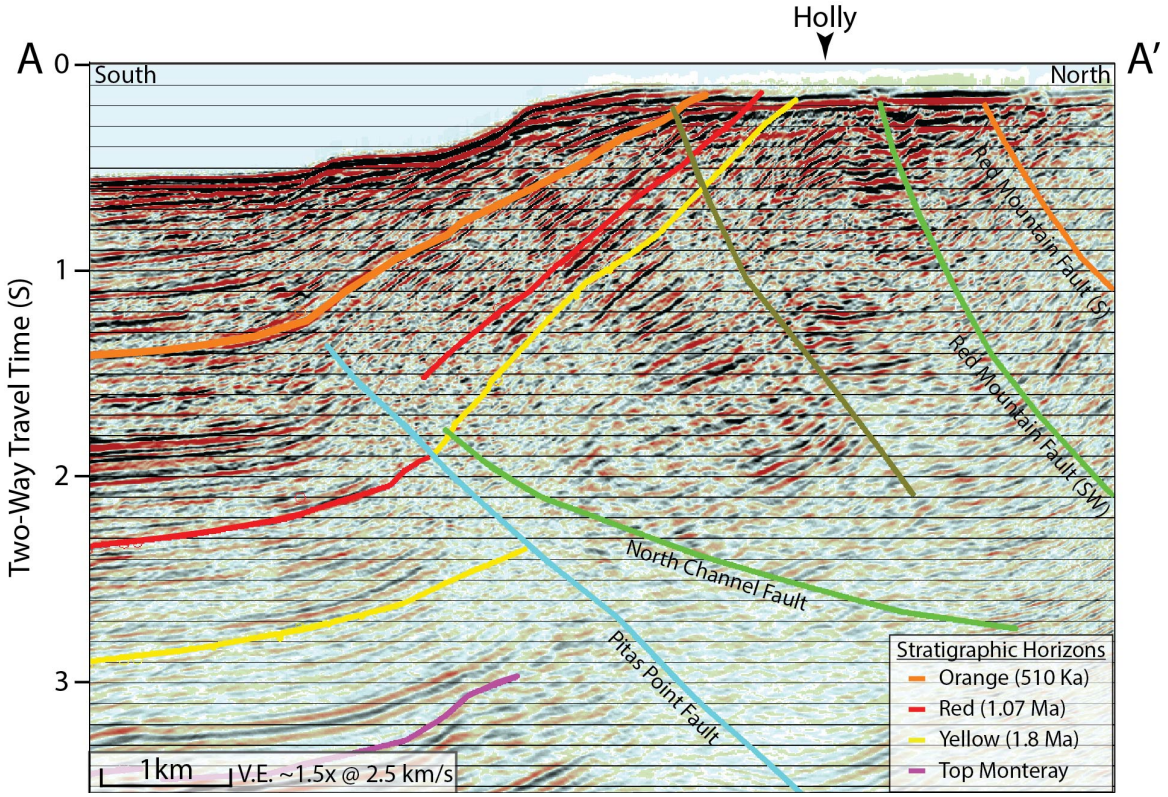

Figure 2.4 2D seismic reflection profile running N-S 1 km west of platform Holly (Figures 1.1A, 5.2) with both stratigraphic (Behl et al., 2016) and fault interpretations (Sorlien and Nicholson, 2015). Survey shows the regional scale faults in proximity to the platform including the Pitas Point, North Channel, Red Mountain (SW), and Red Mountain (S) faults. Both the Pitas Point and North Channel faults are blind, with upper tips at around 2 km depth near platform Holly. The two steeply dipping segments of the Red Mountain Fault show offset of the sea floor within ~1 km of the platform.

2.3. State of stress in southern California

Several previous studies have employed the use of various different stress indicators to provide constraints on crustal stress in southern California. Among all types of indicators, stress orientations from earthquake focal mechanisms make up the majority of available data, constituting 72% of the World Stress Map database (Heidbach et al., 2010). Yang and Hauksson (2013) inverted 179,000 high-quality earthquake focal mechanisms for earthquakes recorded from 1981-2010 and determined maximum horizontal compressive stress orientations and faulting styles across southern California. They note that the regional trend of S_{Hmax} in central to southern California is generally along the NNE direction, with a most likely S_{Hmax} trend of N7°E (Hardebeck and Hauksson, 2001). They also note, however, that several regional and local stress heterogeneities exist at various spatial scales and degrees of heterogeneity, and transition zones from one state of stress to another occur over a distances of only a few kilometers. Similar local scale (<100 km) stress heterogeneities have been identified in dense datasets from around the globe (Heidbach et al., 2010; Montone et al., 2012), and are believed to be controlled by phenomena such as active faulting, gravitational collapse, local intrusions, density contrasts, or detachment faults rather than tectonic sources (Yang and Hauksson, 2013).

The general NNE trend of S_{Hmax}, and the presence of regional and local scale stress heterogeneities in southern California are supported by results from previous borehole breakout studies. Mount and Suppe (1992) observed borehole breakouts in 118 near-vertical wellbores in southwestern California and indicated that S_{Hmax} was generally oriented NE-SW, at a high angle to the San Andreas Fault. However, S_{Hmax} orientations from wellbores within individual basins ranged as much as 50° from one another, and distinct rotations of S_{Hmax} were noted between basins, indicating both regional and local scale stress heterogeneities. Wilde and Stock (1997) observed borehole breakouts in 71 wellbores from six regions in southern California west of the San Andreas Fault and similarly identified a generally NE-SW trend of S_{Hmax}, but also noted the presence of systematic variations in S_{Hmax} orientations both within and between individual basins that indicate strong heterogeneity in the stress field at shallow depths. Furthermore, Wilde and Stock note the presence of anomalous NW directions of S_{Hmax} in certain regions which they believe may be related to structural complexities of nearby fault systems.

2.4. State of stress in the Santa Barbara Channel

The Santa Barbara Channel is one of the more seismically active regions in southern California, and as such, several moderate to large scale earthquakes, including the 1812 M_w >7 earthquake, the 1925 M_w 6.3 Santa Barbara earthquake, and the 1978 M_w 5.1 Santa Barbara earthquake, have been recorded (Bent and Helmberger, 1991). Focal mechanisms from these historical events indicate that they generally occurred as thrust faulting earthquakes with some left-lateral component (Wallace et al., 1981). Similarly, earthquake focal mechanism models from Yang and Hauksson (2013) indicate that the channel is dominated by reverse and strike-slip faulting regimes, but they show considerable spatial heterogeneity between these two regimes. They also show significant heterogeneity in S_{Hmax} orientations, which range from roughly N10°W to N30°E. In comparison with the north Channel region, earthquake density near platform Gail is relatively low. However, at a grid scale of 10 km, and 15 events per grid node, the faulting style and S_{Hmax} orientation are constrained, and indicate the presence of a thrust faulting regime, with an S_{Hmax} orientation between N10°E and N20°E. At platform Holly, denser earthquake coverage allowed for constraint of the faulting style and S_{Hmax} orientation at a grid scale of 5 km and 30 earthquakes per grid node. Focal mechanism results indicate the presence of a thrust faulting regime near platform Holly, but the smaller, denser grid nodes show great heterogeneity in the orientation of S_{Hmax} in the very small area surrounding the platform. The 5 km x 5 km grid node in which Holly is located indicates an S_{Hmax} orientation between N20°E and N30°E. But, platform Holly sits at the southern edge of this grid node, and the neighboring grid node to the south indicates an S_{Hmax} orientation of roughly N10°W. The 30-40° difference in S_{Hmax} orientation between these neighboring two grid nodes illustrates localized stress heterogeneity in the region near Holly, which is likely reflective of the structural complexity in that region (Figures 1.1B, 2.3A).

Previous borehole breakout studies indicate a NE-SW orientation of S_{Hmax} for southern California. However, very few borehole breakout derived stress constraints have been provided within the Santa Barbara Channel itself. Of the 118 boreholes examined by Mount and Suppe (1992), only one well was located within the channel, OCS-P-0231 (OCS) (Figure 1.1A). Results from this well, which is located roughly 20 km south of Santa Barbara in the mid-channel region, indicate an S_{Hmax} orientation of N49°E. Of the 71 wellbores examined by Wilde and Stock (1997), 13 were located within the Santa Barbara Channel, and were actually drilled from platform Holly. However, these wells were highly

deviated, and breakouts occurring in them were not used to constrain the orientation of S_{Hmax}. Wilde and Stock instead applied to these wells an S_{Hmax} orientation of N2°E that was determined from the near-vertical Dreyfus #84 (D84) well (Figures 1.1A, 5.2), which is located onshore and roughly 10 km north of platform Holly. They also provided a rough estimate of the best-fit theoretical stress state, performed by eye, and stated that the breakouts from deviated well sections represented a thrust faulting stress regime. In addition to these two large-scale borehole breakout studies, Heck and Edwards (1998) also provided an estimate of S_{Hmax} from borehole breakouts in the Samedan #2 well of Gato Canyon lease 460 (Figures 1A, 5.2), located roughly 10 km west of platform Holly, which indicated an S_{Hmax} orientation of N32°E. Heck and Edwards also identified preferred fracture strike directions of N25°E and N55°W in this well, which are sub-parallel and sub-perpindicular, respectively, to the principal compression direction of N32°E inferred from borehole breakouts. The sub-perpendicular fractures may indicate that a roughly 87° rotation of S_{Hmax} occurs at certain depths. In total, only 2 borehole breakout derived stress constraints exist within the Santa Barbara Channel itself, and only one study has provided a rough estimate of the stress faulting regime from borehole breakouts. Thus, there is great need for further borehole breakout derived quantitative constraints on stress regimes and S_{Hmax} orientations within the Channel.

2.5. SCEC Community Stress Model

The Southern California Earthquake Center Community Stress Model (SCEC CSM) is a collaborative effort to provide improved constraints on the 4D stress field in southern California by merging together information from borehole measurements, focal mechanisms, GPS strain rates, paleo-slip indicators, topographic loading, geodynamic and earthquake cycle modeling, and induced seismicity into a series of stress and stressing rate models (Hardebeck et al., 2012). The majority of data compiled in the SCEC CSM are derived from focal mechanism inversions and geodetic velocity-based strain rates. However, these methods rely on gridding and interpolation of data, which obscures small-scale heterogeneities (Luttrell and Hardebeck, 2017). On the other hand, several previous studies have noted that borehole breakouts are able to capture stress heterogeneities that occur laterally from well to well, or with depth within a single well. Furthermore, studies have also shown that borehole breakouts are able to capture highly localized perturbations in the crustal stress field that result from faults, fractures, or rock strength and density contrasts (Carminati et al., 2010; Day-Lewis et al., 2010; Kerkela and Stock, 1996; Malinverno et al., 2016; Rajabi et al., 2017; Shamir and Zoback, 1992). Thus, borehole breakouts may capture stress heterogeneities where other methods fall short. Additionally, borehole breakouts are able to provide information on stress in the shallow (<5 km) and aseismic areas of the crust where focal mechanisms are less common (Luttrell and Hardebeck, 2017). Therefore, new borehole breakout derived stress constraints are key to several of the SCEC CSM's major objectives, including improving constraints on stress regimes and their orientations, as well as quantifying stress heterogeneity at a variety of scales.

CHAPTER 3. ANALYSIS OF BOREHOLE BREAKOUT DATA

When a wellbore is drilled, crustal stresses become concentrated at the wellbore wall as circumferential hoop stress. The maximum concentration of hoop stress occurs symmetrically on opposite sides of the wellbore, and when the magnitudes of these stresses exceed the strength of the rock, brittle shear failure occurs, forming spalled regions called borehole breakouts, which elongate the wellbore cross-section into a roughly elliptical shape. In this study, we adhere to the common assumption that one of the principal stresses is vertical, and the other two principal stresses (S_{Hmax} and S_{hmin}) therefore lie in the orthogonal horizontal plane (Bell, 1996; Peška and Zoback, 1995; Snee and Zoback, 2018; Zoback et al., 2003; Zoback, 1992). In a non-deviated wellbore, the vertical stress is oriented parallel to the wellbore cylinder and does not contribute to hoop stress. Thus, the position of maximum hoop stress is determined by the orientations of the two horizontal principal stresses, and borehole breakouts form at the orientation of the minimum horizontal stress (S_{hmin}), which is oriented 90° from S_{Hmax} (Bell and Gough, 1979). In deviated wellbores, however, the vertical principal stress is not oriented parallel to the wellbore, and therefore contributes to the hoop stress. Thus, the position at which borehole breakouts form in non-vertical boreholes is dependent on the orientations and relative magnitudes of all three principal stress components, as well as the orientation of the wellbore itself (e.g. Qian and Pedersen, 1991). In an unchanging stress regime, the position at which borehole breakouts form varies systematically as wellbore orientation changes (see Appendix A3). Therefore, given enough closely spaced boreholes of varying orientations, we are able to determine the relative magnitudes and orientations of all three principal stress components. As we note later, however, breakouts occurring over a wide range of borehole azimuths and deviations are key for a robust constraint on the stress regime.

3.1. Identification of borehole breakouts

In this study, we use oriented 4-arm caliper data to identify and measure the orientations of borehole breakouts. A four-arm caliper tool records the diameter of the borehole at two coplanar axes (C1 & C2), as well the orientation of a single reference pad attached to C1, measured relative to both magnetic north (P1AZ), and to the high side of the borehole (relative bearing - RB) (see Appendix A1). As the caliper tool is pulled up a circular borehole, it rotates freely due to cable torque. However, in a breakout zone, one arm of the caliper tool becomes stuck at the azimuth of borehole elongation, and rotation of the tool ceases. Thus, the orientation of borehole breakouts can be determined from the orientation of the stuck, elongated caliper arm. In order to distinguish the well log responses of borehole breakouts from those produced by other common borehole deformations and tool artifacts (Figure 3.1), we use a set of borehole breakout selection criteria modified from Zajac and Stock (1997).

1. Tool rotation stops in the zone of elongation. This is determined using RB. At platform Gail, we limit maximum variation of relative bearing to less than 10° over 3 m, and limit the sum of clockwise (+) and counterclockwise (-) rotations to less than 5° over 3 m. At platform Holly we loosened constraints to accommodate for noisier data, and limited maximum variation to less than 20° over 3m, and the sum of rotations to less than 10° over 3 m.

2. The larger and smaller caliper arms must be at least 5% different from each other.

3. A) The smaller caliper arm must be less than 1.1x the bit size.
   B) The smaller caliper arm must be greater than the calculated keyseat criterion value (Figure 3.2).

4. The standard deviation of each caliper arm must be less than 1 in (2.54 cm) over a 3 m borehole length.

5. The length of the breakout zone should be at least 3 m for platform Gail, or 1 m for platform Holly to accommodate for noisier data.

The first selection criterion ensures that tool rotation has been obstructed, presumably due to friction with the wellbore wall in a zone of elongation. The second criterion ensures that the borehole has been deformed into a relatively elliptical shape. Criterion 3A is unmodified from Zajac and Stock (1997) and exists to exclude data recorded in the presence of a washout (Figure 3.1), which is a wholesale failure of the wellbore wall that enlarges the borehole in all orientations. In addition to

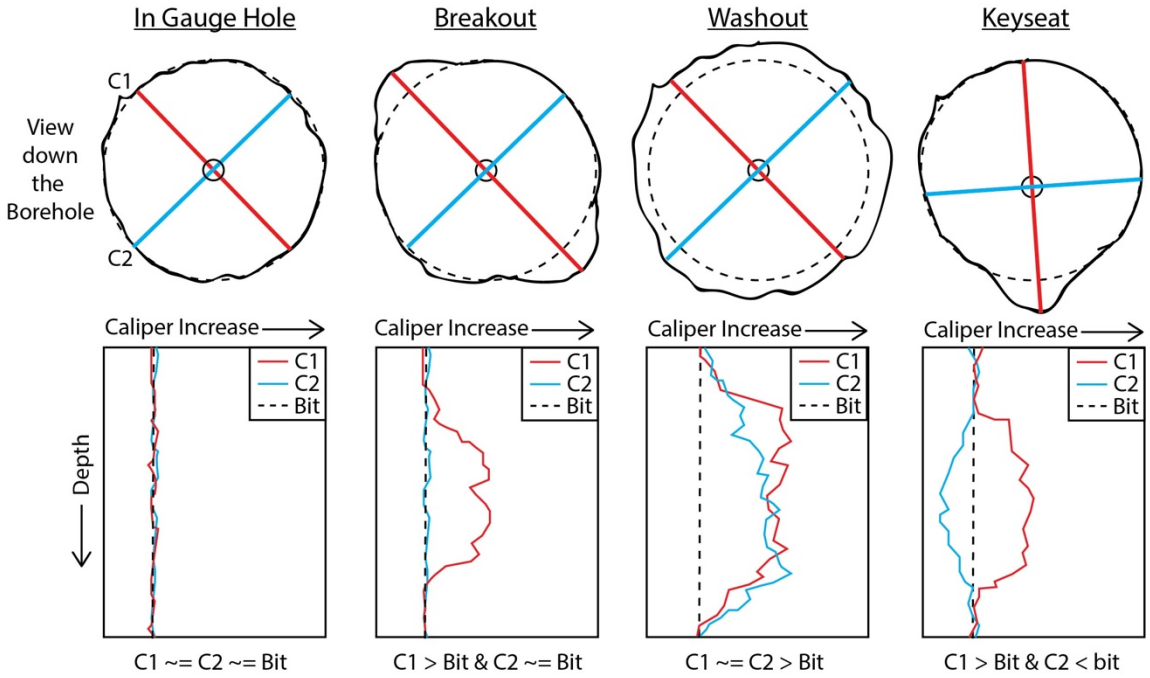

Figure 3.1 Schematic diagram of wellbore cross-sections showing common borehole enlargements and changes in their corresponding caliper curves (C1 & C2) with respect to bit size (Bit). Borehole breakout selection criteria serve to differentiate stress induced borehole breakouts from washouts and keyseats. Sketch based on Reinecker et al. (2003).

criterion 3A, we developed criterion 3B, which excludes data recorded where a keyseat has occurred. A keyseat is a common artifact in 4-arm caliper data that occurs when one arm of the tool digs in to the low side of the wellbore wall, producing a one-sided artificial elongation that can be misidentified as a borehole breakout (Figure 3.1). When a keyseat occurs, the one-sided elongation causes the tool to run off-center, and the smaller caliper arm records a non-diameter chord of the wellbore cross-section that, in the absence of other deformations, is smaller than the size of the drill bit. We use the length of the elongated caliper arm to calculate the expected reduced length of the smaller caliper arm (keyseat criterion value) (Figure 3.2) for a perfectly one-sided elongation. If the smaller caliper arm is less than or equal to this keyseat criterion value the data are excluded. Finally, the fourth and fifth criteria prevent

the inclusion of noisy data and anomalous elongations to ensure that breakouts included in datasets represent only the most consistent and significant zones of elongation.

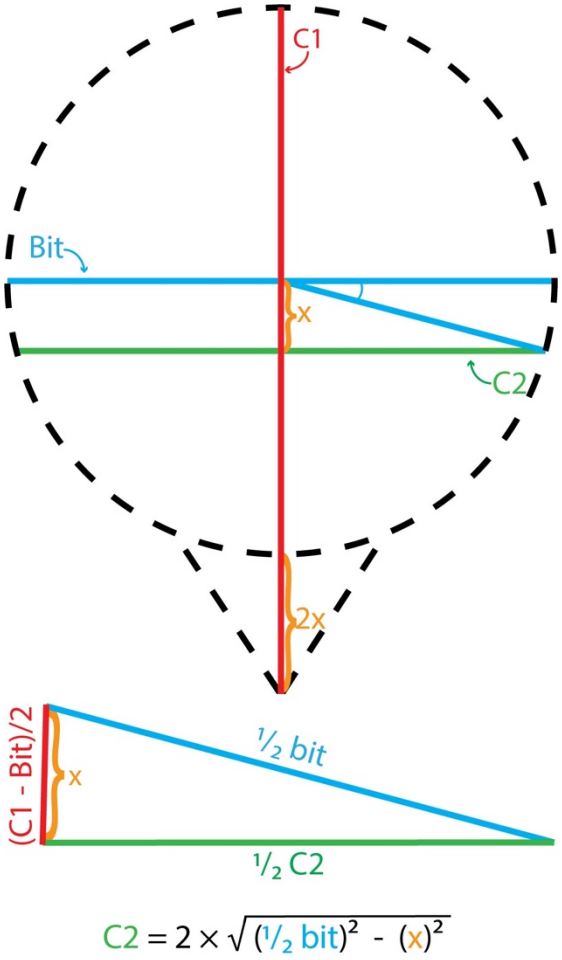

Figure 3.2 Schematic explanation of keyseat identification criterion. In the presence of a keyseat an asymmetrical elongation of C1 puts the caliper tool off center, causing C2 to record a non-diameter chord of the wellbore cross-section. The keyseat criterion uses the length of C1 extension (2x) to calculate the expected reduced length of C2 for the case of a perfectly one-sided elongation in a perfectly circular borehole. For any value of C1 extended beyond the bit size, if the corresponding length of C2 is smaller than or equal to the calculated "keyseat value" of C2 (above), the elongation is considered to be a keyseat, and is excluded from borehole breakout selection.

3.2. Averaging borehole breakout data

The 4-arm caliper data used in this study are recorded as discrete data points at 0.5 ft (0.1524 m) logging increments. Once all breakout criteria are met, a mean depth value, as well as circular mean values for the breakout elongation orientation, borehole azimuth, and borehole deviation are obtained such that each separate breakout zone can be defined by a single value of each (see Appendix A4). The primary benefit of this step is reduction in computation time. We used the LSU HPC SuperMIC supercomputer to allocate computation for each borehole breakout dataset across 5 nodes with 20 processors per node. Averaging breakout data points at platform Gail reduced the number of theoretical breakout orientations to be calculated per forward model from 7571 to 148. Across all calculations,

averaging breakout data reduced computation time from ~7031 hrs CPU time (wall time ~122 hrs) to ~575 hrs CPU time (wall time ~ 10 hrs). Additionally, averaging breakouts helps to deal with certain shortcomings of the 4-arm caliper tool. In cases where cable torque causes the tool to ride along one edge of the breakout, or to rotate slowly, but continuously within a breakout, averaging data points should provide a more accurate representation of the breakout's midpoint.

3.3. Determination of best-fit stress regime and S_{Hmax} orientation

We have developed a new misfit-based forward modeling technique based on that of Zajac and Stock (1997) that allows us to quantitatively constrain the best fit stress regime and S_{Hmax} orientation for a given area using borehole breakouts in closely spaced, differently oriented wellbores. Once borehole breakouts have been identified and averaged, we use the wellbore orientations (hole azimuth and deviation) at which each observed breakout occurred to calculate sets of corresponding theoretical borehole breakout orientations for a wide range of stress regimes and regime orientations. We then use a one-norm misfit calculation to determine the average angular misfit between each set of theoretical breakout orientations and the original set of observed breakout orientations, and select the stress regime and S_{Hmax} orientation of the misfit-minimizing set of theoretical breakouts as the best-fit stress parameters for the given dataset. Finally, we use bootstrap resampling to resample the original set of observed borehole breakouts 100 times, and compile the misfit minimizing stress regimes and S_{Hmax} orientations from each to provide a range of high-confidence stress constraints for the region.

3.3.1. Parameterization of stress state

The unrestricted principal stress tensor is completely described using six parameters. Three of these parameters describe the magnitudes of the principal stress components S1, S2 and S3 and the other three are the Euler angles (α, β, γ) which describe three successive rotations of the stress tensor about various axes to completely describe its orientation (Zajac, 1997). Operating under the assumption of a vertical principal stress, however, restricts rotation of the stress tensor to a single degree of freedom about the vertical, or z-axis, and we are therefore able to describe the complete stress tensor using only four parameters: the magnitudes of the three principal stresses (S_{Hmax}, S_{hmin}, and S_V), and a single Euler angle (α) which describes the clockwise rotation from north of S_{hmin} (90° from S_{Hmax}) about the vertical, or z-axis in the horizontal plane (see Appendix A5, A6).

3.3.2. Selection of represented stress regimes and regime orientations

The suite of discrete sets of theoretical borehole breakout orientations to which observed borehole breakout orientations are compared must represent a full range of possible stress regimes, as well as all possible horizontal stress orientations of each. To represent a full range of possible stress regimes, we allow the magnitude of each principal stress component to vary from 1.0 - 2.0 in increments of 0.1 such that there are 11 possible values for each. We then determine all unique numerical combinations of the three principal stress values, excluding those that are either illogical ($S_{Hmax} > S_{hmin}$) or unlikely ($S_{Hmax} = S_{hmin} = S_V$), and are left with 715 unique principal stress magnitude combinations that represent a range of normal, oblique normal, strike-slip, oblique reverse, and reverse faulting stress regimes. Then, we represent all possible horizontal stress orientations of each regime by varying the Euler angle (α). The stress tensor exhibits 2-fold rotational symmetry in the horizontal plane, so we

allow the Euler angle (α) to vary from 0 - 180° in 1° increments (See Appendix A5). Thus, a discrete set of theoretical borehole breakout orientations is calculated for each of the 715 principal stress magnitude combinations at 180 different horizontal stress orientations, resulting in 128,700 sets of theoretical borehole breakout orientations to which original borehole breakouts orientations are compared.

3.3.3. Calculation of theoretical breakout orientations

In order to properly represent the effects of each stress regime and regime orientation on arbitrarily oriented boreholes, we use tensor transformation equations (see Appendix A6) from Zoback (2007) to rotate the far field principal stress tensors into the borehole coordinate system. Then, using equations developed by Hiramatsu and Oka (1962) and Fairhurst (1968) (see Appendix A7), we are able to use the wellbore orientations (hole azimuth and deviation) at which observed borehole breakouts occurred to calculate the orientations at which borehole breakouts would theoretically form at the same wellbore orientations under each of the 128,700 stress conditions.

3.3.4. Misfit calculation

Once all sets of theoretical breakout orientations have been calculated, we use a one-norm average angular misfit calculation to determine the best-fit stress regime and regime orientation (Parker and McNutt, 1980; Zajac, 1997).

$$M^1 = \frac{1}{n}\sum_{j=1}^{n}|\theta_j - o_j|$$

Where n is the total number of observed borehole breakouts, o_j is the orientation of the j-th observed breakout, and θ_j is the theoretical breakout orientation calculated for the wellbore orientation of the j-th breakout for a given stress regime and regime orientation. The parameters of the set of theoretical borehole breakouts that exhibit the least angular misfit from the original set of observed borehole breakouts are then determined to represent the best-fit stress regime and S_{Hmax} orientation for the given dataset.

3.3.5. Bootstrapping of data

In order to ensure confidence in the results of our forward modeling misfit calculation we use bootstrap resampling to resample each of our original borehole breakout datasets 100 times, such that within each resampled dataset individual breakouts may be included multiple times, while others may be excluded (see Appendix A8). After the bootstrap sample datasets have been generated, we compute the best-fit stress regime and S_{Hmax} orientation of each. This approach allows us to determine if there are any underlying patterns in the data that may remain unresolved by only forward modeling the original dataset. All 100 best-fit stress regimes and their S_{Hmax} orientations are then compiled to represent a range of high-confidence stress constraints for the original borehole breakout dataset.

CHAPTER 4. RESULTS

4.1. Presentation of borehole breakout orientations

To view the borehole breakout results and compare them to theoretical breakout orientations, breakouts are traditionally plotted on an equal angle, lower hemisphere stereographic projection plot (Mastin, 1988); we instead use a polar projection (Figures 4.2, 4.5). Each borehole breakout is plotted as a single tick mark with the same orientation as the borehole elongation in a "looking down the borehole" system (Peska and Zoback, 1995). The location of the tick mark on the plot is determined by the borehole azimuth and deviation where the breakout occurs. Borehole deviation increases outward from the center of the plot, with data from vertical boreholes plotted at the center, and data from horizontal holes plotted on the periphery. Borehole azimuth changes radially around the plot (see Appendix A2).

4.2. Stress ratio (ϕ) and aphi (A_ϕ):

For simplicity in displaying the results, we further parameterize each of the 715 unique principal stress magnitude combinations using the stress ratio (ϕ) which we define as

$$\phi = \frac{S_1 - S_2}{S_1 - S_3}$$

where S_1 is the maximum compressive stress, S_2 is the intermediate stress, and S3 is the minimum compressive stress. The 715 combinations of S_{Hmax}, S_{hmin}, and S_V used in this study represent 33 unique stress ratio values between 0 - 1.0 (see Appendix A9). Stress ratios close to 0 and 1.0 indicate $S_1 \sim S_2$ and $S_2 \sim S_3$, respectively. It is important to note, however, that any two principal stress magnitude combinations with the same value of ϕ may represent different faulting regimes depending on the orientations of S1, S2 and S3. Thus, values of ϕ are more descriptive when converted to A_ϕ, which captures both ϕ and the style of faulting that each principal stress relative magnitude combination represents. We define A_ϕ as:

$$A_\phi = \begin{cases} \phi & if\ S_3\ is\ most\ vertical\ (reverse) \\ 2 - \phi & if\ S_2\ is\ most\ vertical\ (strike - slip) \\ 2 + \phi & if\ S_1\ is\ most\ vertical\ (normal) \end{cases}$$

A_ϕ values from 0-1 represent reverse faulting, values from 1- 2 represent strike-slip, and values from 2 - 3 represent normal faulting. It is also important to note that any two principal stress magnitude combinations with identical A_ϕ values (same ϕ and stress faulting regime), but different absolute principal stress magnitude values, may produce slightly different theoretical breakout orientations. Thus, the misfit value for a thrust faulting stress regime with S_{Hmax} = 1.8, S_{hmin} = 1.4, and S_V = 1.0 (ϕ = 0.5; A_ϕ = 0.5) may be slightly different that from a regime with S_{Hmax} = 1.2, S_{hmin} = 1.1, and S_V = 1.0 (ϕ = 0.5; A_ϕ = 0.5) despite having identical ϕ and A_ϕ values.

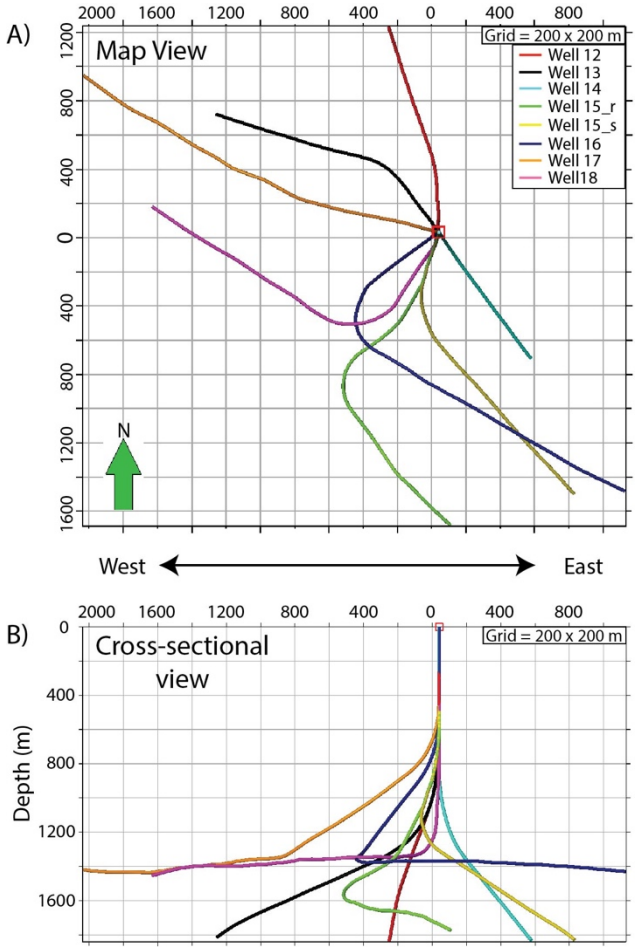

Figure 4.1 A) View of platform Gail well paths from directly overhead showing the spatial extent of wellbores. The furthest wellbore, Well 17, reaches roughly 2200 m NW from the platform. B) Cross-sectional view of platform Gail well paths looking horizontally from S to N showing the depth coverage of the wellbores. The maximum well depth is just over 1700 m TVD.

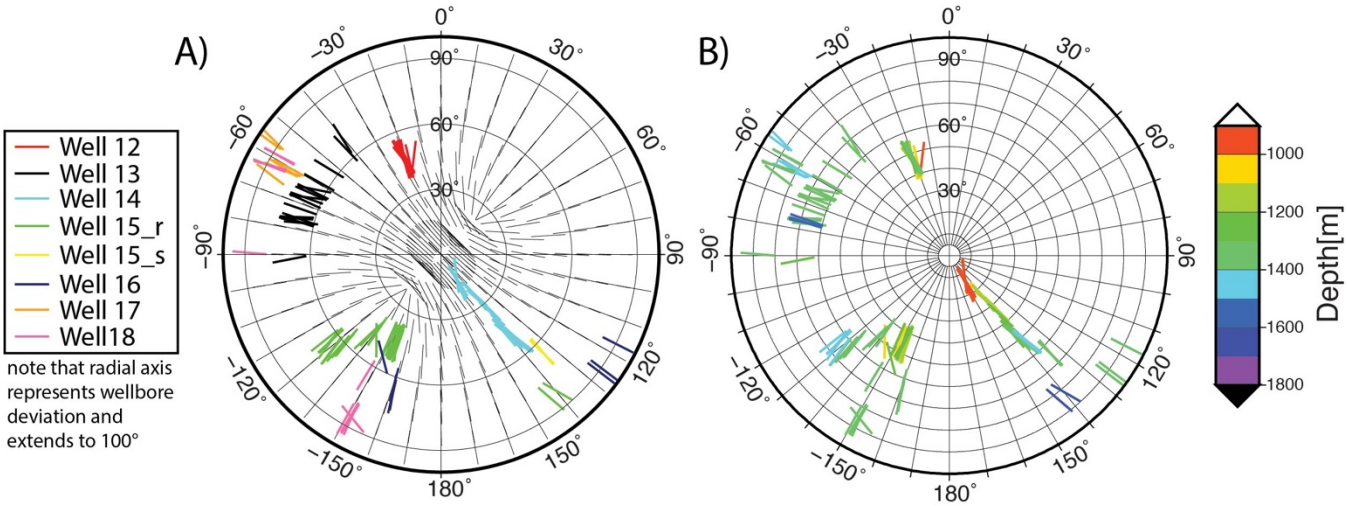

Figure 4.2 A) Polar plot of platform Gail breakout orientations color-coded by individual wells plotted on top of black sticks that represent the theoretical best-fit stress state (see Figure 4.3). B) Platform Gail breakout orientations with each breakout color-coded by true vertical depth.

4.3. Platform Gail results

We analyzed eight deviated wells from platform Gail where recorded depths ranged from 790 – 1770 m (See Appendix A10) TVD (true vertical depth), with depth ranges of individual wells shown in Figure 4.1B. Three wellbores were logged at deviations less than 10°, but no breakouts were identified in these well sections, and we were therefore unable to obtain an estimate of the orientation of S_{Hmax} based on data from these near-vertical sections. We did, however, identify six sections of breakouts in Well 14 at deviations ranging from 11 - 16° (depth range 951 - 986 m TVD) (Figure 4.2A,B) with a circular mean breakout orientation of N157.76°E and a standard deviation of 12.1°. Studies of the effects of borehole deviation on breakout azimuth indicate that breakouts at deviations of less than 20° in thrust faulting conditions have a greater than 88% likelihood of forming within 10° of the azimuth of the minimum horizontal stress (Mastin, 1988). Thus, these breakouts could potentially be taken to indicate an S_{Hmax} orientation of N67.76°E $\pm$ 12.1°. In addition to these six sections of breakouts, we also identified 142 continuous breakout zones in wellbore sections deviated from 23° to 96° (depth range 986 - 1652 m TVD) (Figure 4.2A,B), which, in combination with the others, allowed us to constrain both the orientations and relative magnitudes of all three principal stress components beneath the platform using our misfit based forward modeling technique.

Borehole breakouts in deviated wellbores beneath platform Gail tended to show a radial pattern (Figure 4.2A,B), indicating a tendency for breakouts to form aligned with the high and low sides of the borehole. While there is some concern that these deformations could in some instances result from tool drag, measures were taken during the breakout selection process to ensure that deformations were stress induced and not due to other factors. Several past studies have simply excluded radial breakouts from stress analysis (e.g. Plumb and Hickman, 1985) but this practice creates gaps in breakout plots that are typically sparse to begin with and also introduces bias in the constraint of the stress ratio (ϕ) and the orientation of maximum compressive stress. Many stress states include borehole orientations at which breakouts are expected to form radially (See Appendix A13) (e.g., Mastin, 1988; Peška and Zoback, 1995), and it is therefore especially important that these breakouts be selected carefully and included in stress analyses.

Misfit calculations between our original set of observed borehole breakouts and all sets of theoretical breakout orientations (Figure 4.3A) indicate a thrust faulting stress regime (S_H = 1.7; S_h = 1.6; S_V = 1.0) with a stress ratio of 0.14 (A_ϕ = 0.14), and an S_{Hmax} orientation of N45°E. Additionally, all 100 bootstrap samples of the original platform Gail data indicate a thrust faulting regime ($S_H > S_h > S_V$). Possible stress ratios from bootstrap sample datasets ranged from 0.1 to 0.2, with a median value of 0.17 (Figure 4.3C), and possible S_{Hmax} orientations ranged from N40°E to N55°E with a median value of N44°E (Figure 4.3B). Therefore, our results from the original set of observed borehole breakouts represent very high confidence constraints on the stress regime and S_{Hmax} orientation beneath platform Gail. As such, we place higher confidence in the N45°E S_{Hmax} orientation from misfit calculations than the N67.76°E $\pm$ 10 S_{Hmax} orientation from breakouts in near vertical wellbore sections, as the misfit calculation is based on 148 breakouts, while the latter is based on only 6. Thus, our results indicate the presence of a thrust faulting stress regime with a N45°E orientation of S_{Hmax} beneath platform Gail.

It is also important to note that in some platform Gail wells we have identified wellbore sections where caliper lengths indicate the presence of a borehole breakout, but tool rotation is not obstructed, and instead varies back and forth continuously between two clear extrema, which we believe may

represent the edges of wide breakout zones (see Appendix A12). In these cases, our borehole breakout criterion may select separate zones at the edges of wide breakouts, where tool rotation changes directions, but not between the edges where the tool rotates freely. While we do not average these separate breakout zones, we note that doing so could produce a more accurate representation of the midpoint of a wide breakout. Furthermore, we note that the range of rotation between the two breakout edges could allow for estimation of breakout width, which when combined with estimates of rock strength, can be used to obtain an estimate of the absolute magnitude of S_{Hmax}, a valuable parameter in the quantitative assessment of fault slip potential (Vernik and Zoback, 1992).

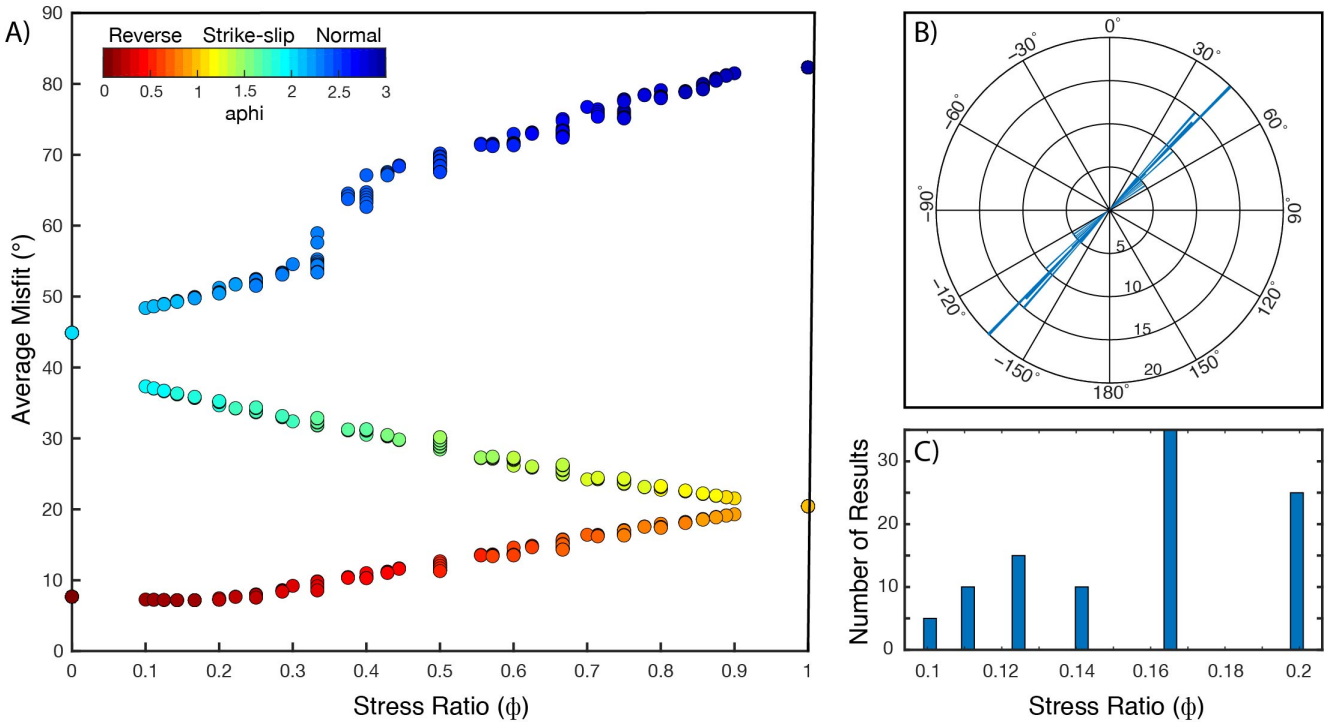

Figure 4.3 A) Misfit between observed borehole breakouts at platform Gail and theoretical breakout orientations from the best-fit S_{Hmax} orientation for each of the 715 represented stress regimes. The best-fit stress state is a thrust faulting stress regime (S_{Hmax} = 1.7; S_{hmin} = 1.6; S_V = 1.0) with a stress ratio of 0.14 and an S_{Hmax} orientation of N45°E. B) Rose plot of S_{Hmax} orientations of the best-fit stress regimes obtained from 100 bootstrap datasets, which ranged from N40°E to N55°E with a median of N44°E. C) Histogram of stress ratios of best-fit stress regimes from 100 bootstrap datasets, which ranged from 0.1 to 0.2, with a median of 0.17. Gaps in the histogram are stress regimes that were not represented by the 715 relative magnitude combinations used in this study (see Appendix A9).

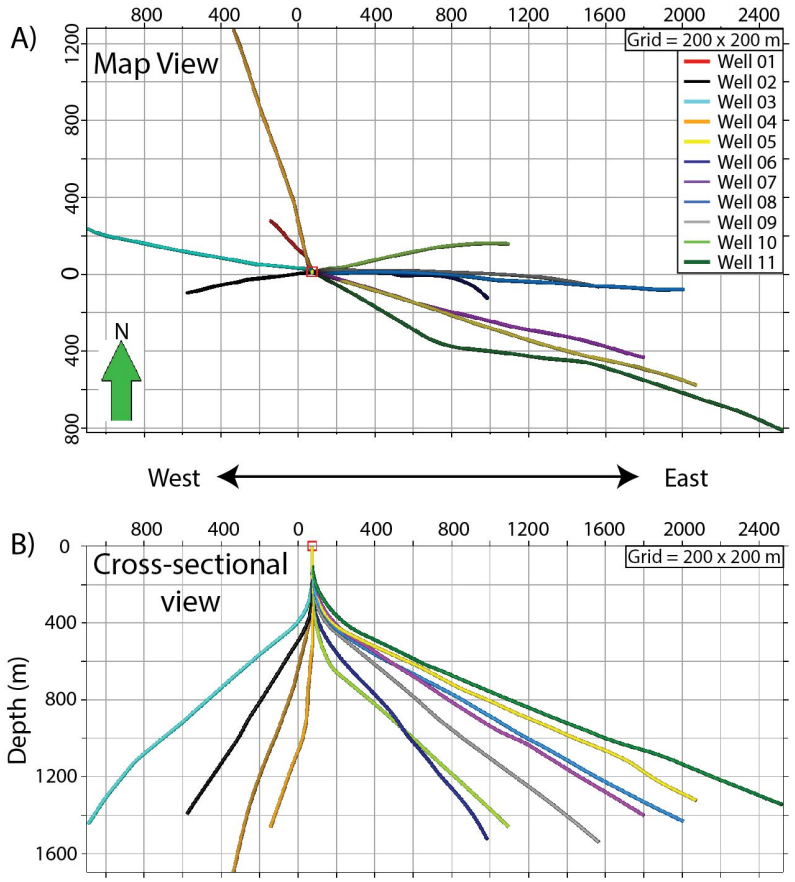

Figure 4.4 A) View of platform Holly well paths from directly overhead showing the spatial extent of wellbores. The furthest wellbore, Well 11, reaches over 2500 m SE from the platform. B) View of platform Holly well paths looking horizontally from S to N, showing the depth coverage of the wellbores. The maximum well depth is roughly 1700 m TVD.

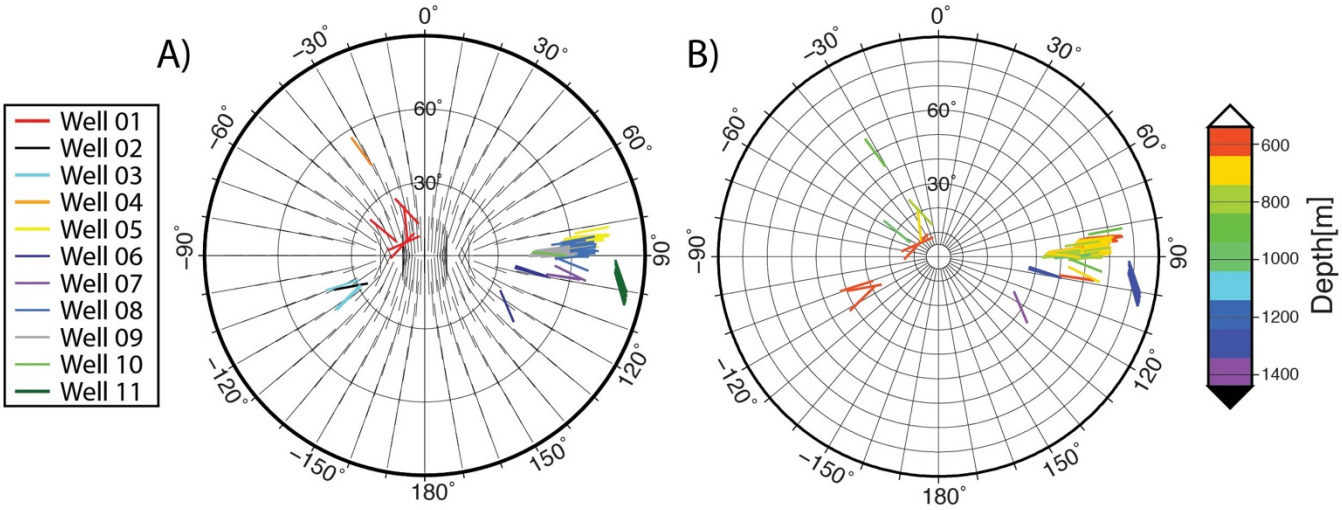

Figure 4.5 A) Polar plot of platform Holly breakout orientations color-coded by individual wells plotted on top of black sticks that represent the theoretical pattern for the best-fit stress state (see Figure 4.6). Concentric grid circles represent borehole deviation at 30° intervals. B) Polar plot of platform Holly breakouts color-coded by true vertical depth.

4.4. Platform Holly results

We also analyzed 11 deviated wells from platform Holly where recorded depths ranged from 545 – 1590 m TVD (see Appendix A11), with depth ranges of individual wells shown in Figure 4.4B. We identified two sections of borehole breakouts in Well 01 from this platform that occurred at near-vertical wellbore deviations, and were therefore useful in constraining the orientation of the maximum horizontal principal stress. These breakouts occurred at a mean deviation of 10.01° (depth range 557 - 568 m TVD) (Figure 4.5A,B) and indicated a circular mean S_{Hmax} orientation of N35.88°W with a standard deviation of 16.1°. We also identified three sections of borehole breakouts in this same well that occurred at deviations ranging from 15° to 20° (depth range 645 - 991 m TVD) (figure 4.5A,B) and indicated a circular mean S_{Hmax} orientation of N56.76°E with a standard deviation of 24.3°. In addition to these 5 breakouts, we identified 84 continuous breakout zones in wellbore sections deviated from 32° to 80.8° (depth range 550 - 1405 m TVD) (Figure 4.5A,B), which we used in combination with the others to constrain both the orientations and relative magnitudes of all three principal stress components beneath the platform. These breakouts, however, occurred at a limited range of borehole azimuths and deviations, leading us to question whether or not data coverage at platform Holly is complete enough to produce robust constraints on the stress regime and S_{Hmax} orientation from our misfit based forward modeling approach.

Misfit calculations between our original set of observed borehole breakouts and all sets of theoretical breakout orientations indicate a thrust faulting stress regime (S_{Hmax} = 2.0; S_{hmin} = 1.9; S_V = 1.0) with a stress ratio of 0.10, and an S_{Hmax} orientation of N75°W (Figure 4.6A). Additionally, all 100 bootstrap samples of the original platform Holly data indicate a thrust faulting stress regime. Possible stress ratios from bootstrap sample datasets ranged from 0 to 0.3 with a median value of 0.1 (Figure 4.6C), and possible S_{Hmax} orientations ranged from N37°W to N116°W, with a median value of N74°W (Figure 4.6B).

While our constraint of a thrust faulting regime at platform Holly is consistent with the roughly-estimated best fit stress regime provided for Holly by Wilde and Stock (1997), further inspection of our numerical results indicates that the azimuthal distribution of breakouts was not wide enough to produce robust quantitative constraints on the stress regime or S_{Hmax} orientation. In comparison with platform Gail, where a larger number of breakouts were identified at a wide range of borehole azimuths and deviations (Figure 4.2A,B), the average angular misfit values for non-best-fit stress states at platform Holly increase very slowly as A_ϕ varies from 0 - 2.0 (Figure 4.6A). The best-fit strike-slip stress regime for the platform Holly data is just 2.38° different from the overall best-fit regime, and the entire range of stress states with A_ϕ ranging between 0 - 2.0 falls within 5.72° average angular misfit of the overall best-fit regime. The closeness in misfit results between these regimes and the best-fit regime for platform Holly stems from the fact that 79 of the 89 breakouts identified occurred in wellbores that were drilled at azimuths between N81°E and N99°E. Furthermore, the majority of these breakouts formed on the high and low sides of the borehole, such that their orientations are plotted radially on the polar plot (Figure 4.5A,B).

All theoretical plots for stress regimes with A_ϕ between 0 - 2.0 have a range of borehole azimuths at which breakouts are expected to form radially. The width of this azimuthal range decreases from A_ϕ = 0, where all breakouts are expected to form radially regardless of hole azimuth or deviation,

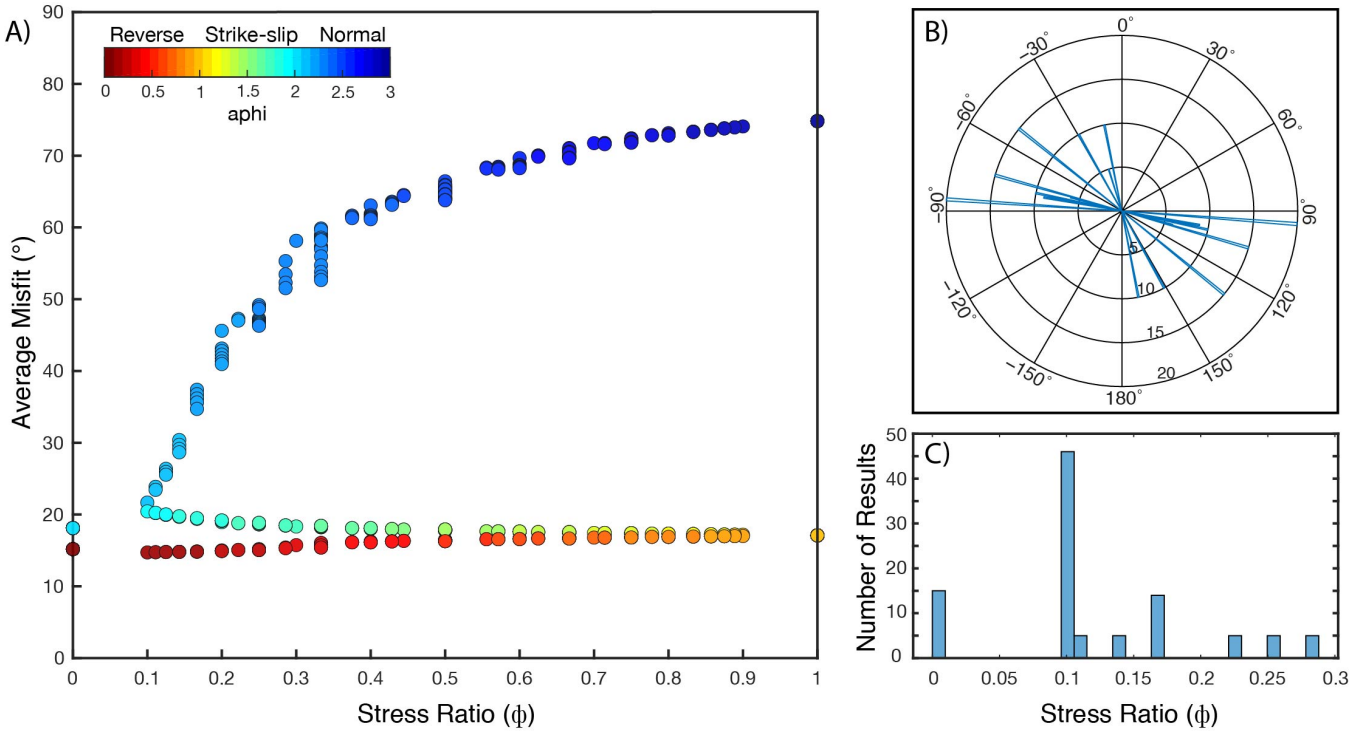

Figure 4.6 A) Misfit between observed borehole breakouts at platform Holly and theoretical breakout orientations from the best-fit S_{Hmax} orientation for each of the 715 represented stress regimes. A range of low misfit values is obtained for reverse, oblique reverse, and strike-slip faulting stress regimes indicating that poor azimuthal coverage of breakouts (see Figure 4.5A,B) may limit our ability to provide a unique determination of the stress regime and S_{Hmax} orientation. In the shallow near-vertical parts of Well 01, the S_{Hmax} orientation is N35.88°W, and N56.76°E at depth (see Figure 4.5A,B). B) Rose plot of S_{Hmax} orientations of the best-fit stress regimes obtained from 100 bootstrap resampled datasets. C) Histogram of stress ratios of best-fit stress regimes from 100 bootstrap datasets. Gaps in the histogram are stress regimes that were not represented by the 715 relative magnitude combinations used in this study (see Appendix A9).

to A_ϕ = 2.0, where breakouts form radially regardless of deviation at only a single orientation, and rotate away quickly as borehole azimuth changes (see Appendix A13). Thus, given mostly radial breakouts at a narrow range of borehole azimuths, a large range of stress regimes with A_ϕ ranging between 0-2.0 may exhibit relatively low misfit values at a range of S_{Hmax} orientations, resulting in poor constraint of the best fit stress regime and S_{Hmax} orientation at platform Holly.

While more breakouts at a wider range of borehole azimuths would be necessary to produce robust quantitative constraints on the stress regime at platform Holly, our results do narrow down the possibilities to either a reverse, oblique reverse, or strike-slip faulting regime (Figure 4.6A). Additionally, Wilde and Stock (1997) identified mostly radial borehole breakouts in 13 wells from platform Holly. Log data from 4 of these wells were included in our analysis as Well 04, Well 06, Well 07, and Well 08 (3120_15, 3242_11, 3242_12, 3242_15, respectively, in Wilde and Stock (1997)). However, the other 9 wells from their dataset were not included in our analysis, and these wells included breakouts at borehole azimuths from N100°E to N120°E, from N30°W to N70°W, and from N90°W to N110°W, that support the presence of a thrust faulting regime with A_ϕ between 0-1.0 (see Appendix

A14). As far as the orientation of S_{Hmax}, we are unable to rely on the results of our misfit based forward modeling technique. We instead rely on S_{Hmax} constraints from borehole breakouts identified in near-vertical wellbore sections which suggest a shallow S_{Hmax} orientation of N35.88°W, and an S_{Hmax} orientation at depth of N56.76°E.

CHAPTER 5. DISCUSSION

5.1. Platform Gail

Our analysis of borehole breakouts at platform Gail indicates a thrust faulting stress regime with a stress ratio (ϕ) of 0.14 (bootstrap confidence range 0.1 - 0.2) and a maximum compressive stress direction of N45°E (bootstrap confidence range N40°E - N55°E) (Figure 4.3A). While no other studies have analyzed borehole breakouts in the immediate vicinity of platform Gail, both Mount and Suppe (1992) and Wilde and Stock (1997) observed borehole breakouts onshore in the nearby Oxnard Plain, which is located in the Central Ventura Basin roughly 20-30 km northeast of platform Gail (Figure 5.1). Although neither study constrained a stress regime for their respective areas, both were able to constrain orientations of maximum compressive stress from borehole breakouts in vertical wellbore section. Mount and Suppe (1992) used the borehole breakout identification criteria from Plumb and Hickman

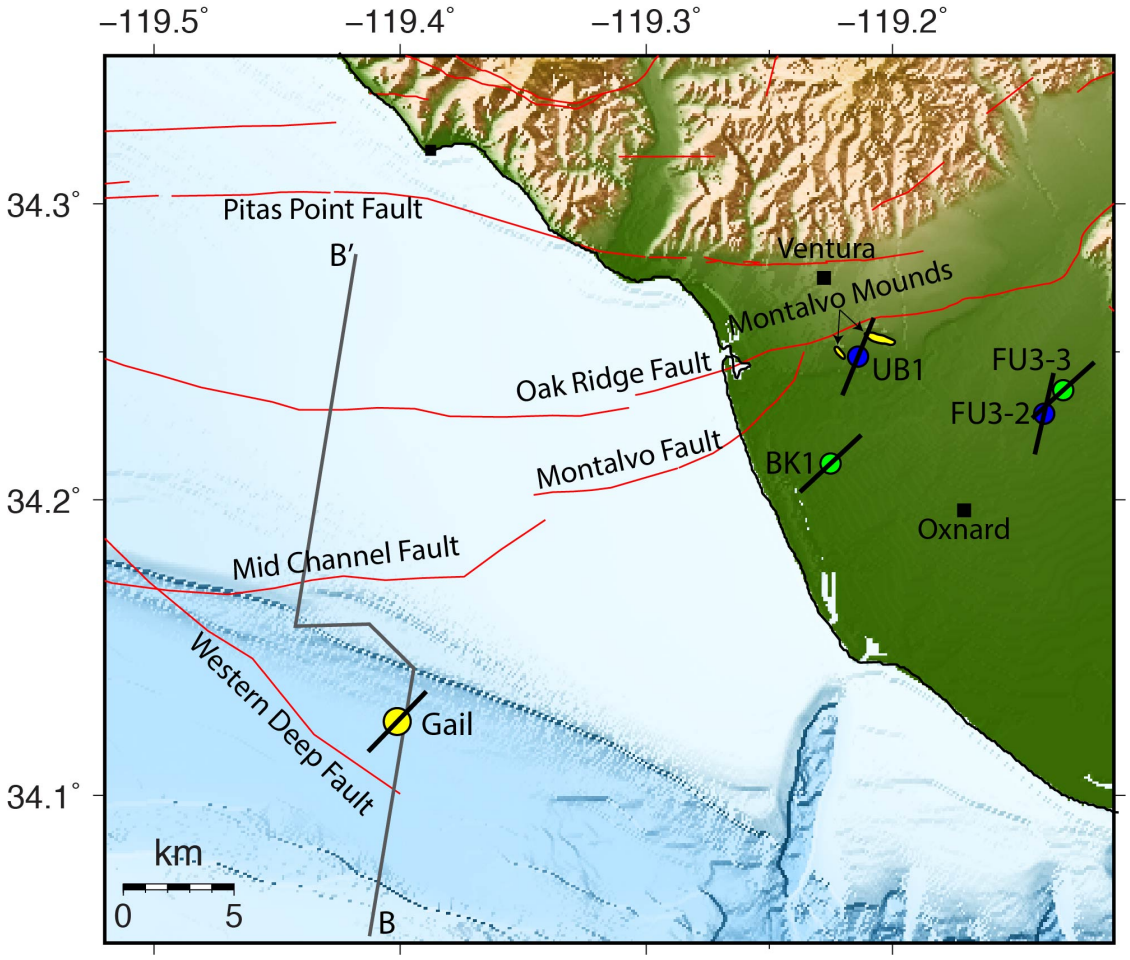

Figure 5.1 Map showing platform Gail (yellow circle) and onshore Oxnard Plain well locations with borehole breakout derived S_{Hmax} orientations shown by black lines, regional scale faults shown in red, and the path of the composite 2D seismic profile B - B' shown with a grey line (see Figure 2.2 for the profile). Mount and Suppe (1992) Freidrich Unit 3-2 (FU3-2) and Utsaki-Burns 1 (UB1) are shown with blue circles, and Wilde and Stock's Ballard Kramer 1 (BK1) and Freidrich Unit 3-3 (FU3-3) wells are shown with green circles. The NE-trending Montalvo Mounds are highlighted in yellow (Fisher et al.,

(1985) to identify breakouts in 118 wells in the larger southwestern California region. Of the wells in their dataset, the two located closest to platform Gail were Friedrich unit 3-2 and Utsaki-Burns 1 of the Oxnard Plain, which exhibited S_{Hmax} orientations of N22°E and N13°E respectively (Figure 5.1). While these results are consistent with an overall NE-SW regional trend of S_{Hmax}, they are rotated 23° and 32° counterclockwise from the S_{Hmax} orientation we determined for platform Gail. This difference in orientations may reflect heterogeneity in the orientation of S_{Hmax}, but it could also be reflective the authors' use of dated breakout identification criteria, which have since been modified and improved by several studies including our own. Wilde and Stock (1997) modified the breakout identification criteria of Plumb and Hickman (1985) to more rigorously exclude elongations due to washouts, pinch-ins of the hole, and tool malfunctions. Additionally, they excluded all breakouts shorter than 10 ft, ensuring that only the most significant deformational trends were included in their analysis. Using these modified criteria, Wilde and Stock (1997) identified borehole breakouts in two wells from the Oxnard Plain, Friedrich Unit 3-3 and Ballard Kramer 1 (Figure 5.1), which indicated S_{Hmax} orientations of N48°E and N47°E respectively (Figure 5.1). Their results are within 3° and 2° of the S_{Hmax} orientation that we have constrained beneath platform Gail, indicating that the orientation of maximum compressive stress is potentially laterally continuous throughout the area which includes both platform Gail and the Oxnard Plain.

The orientations of maximum compressive stress constrained beneath platform Gail and the Oxnard plain are further supported by both localized and regional structural trends present at each of these locations. Platform Gail, for example, sits just north of the S-dipping, NW-striking Western Deep Fault (Figure 2.1A), which is a blind, regional scale thrust fault with shallow deformation expressed as folding rather than fault offset (Figure 2.2). On a more local scale, wells from the platform target the Sockeye Anticline structure, which is a broad, NW-trending, doubly plunging anticline bound to both the north and southwest by S-dipping, NW-striking thrust faults (Figure 2.1B) (Sankur et al., 1990). Thus, our assertion of a thrust faulting stress regime with an S_{Hmax} orientation of N45°E is consistent with the local compressive structures of the Sockeye anticline, which are reflective of the deeper regional trend of the Western Deep Fault.

The wells from Wilde and Stock (1997) and Mount and Suppe (1992) discussed above target two separate oil fields within the Oxnard Plain, with each study containing one well from each of the fields. Friedrich Unit 3-3 from Wilde and Stock (1997) and Friedrich Unit 3-2 from Mount and Suppe (1992) both target the Santa Clara Avenue Oil Field, while Wilde and Stock's Ballard Kramer 1 and Mount and Suppe's Utsaki-Burns 1 both target the West Montalvo Oil Field. The Santa Clara Avenue Oil Field is a stratigraphically trapped reservoir (DOGGR, 1992), and therefore does not contain any major structural trends with which the orientation of maximum compressive stress can be correlated. However, the West Montalvo Oil field wells target the E-W trending Montalvo anticline, which is bound to the north by a steeply S-dipping, NE-trending segment of the Oak Ridge Fault, and is cut by a steeply N-dipping, NE-trending growth fault called the Montalvo Fault (Figure 5.1) (Johnson et al., 2017; Yeats, 1976). While both Wilde and Stock (1997) and Mount and Suppe (1992) were unable to constrain the stress regime beneath their West Montalvo Oil Field wells, several studies have proposed that the Montalvo Mounds, which are two short-wavelength pressure mounds overlying the buried eastern tip of the Oak Ridge Fault (Figure 5.1), may indicate recent and ongoing left or left-oblique slip along the Oak Ridge Fault, Montalvo Fault, and other fault splays in the area (Fisher et al., 2005; Johnson et al., 2017; Yeats, 1976). The Montalvo Mounds trend NW-SE, and are potentially cored by shallow thrust faults (Fisher et al., 2005). In a strike-slip stress regime, the NE-SW orientations of S_{Hmax} from both studies are consistent

with these local structural trends in that S_{Hmax} is oriented at a low angle to the fault planes of the potentially strike-slip or oblique reverse, NE-striking Oak Ridge and Montalvo Faults, and is oriented at a high angle to the fold axis of the compressive NW-trending Montalvo Mounds.

Our constraints on S_{Hmax} beneath platform Gail and the results from previous studies beneath the Oxnard Plain are consistent with interpretations of regional and local scale structures at each location. This consistency provides confidence in our method, which utilizes breakouts in deviated wellbores to constrain the stress regime and orientation of S_{Hmax}. In the case of Gail, the area sampled by the wells is 3.2 km x 2.9 km (Figure 4.1A), which we take to at least represent the stress regime of the Sockeye Anticline structure shown in Figure 2.1B. However, we are cautious about ubiquitously extending Gail's stress regime as far as the Oxnard plains even though S_{Hmax} in this larger region shows similar orientations, as results in the Oxnard Plain indicate in part an oblique- or strike-slip regime. We also note that stress regimes determined from focal mechanism show more lateral variability in the Southern California than do the stress orientations we have observed from borehole breakouts (Yang and Hauksson, 2013).

5.2. Platform Holly

At platform Holly, poor borehole breakout data coverage limited our ability to provide robust quantitative constraints on the stress regime and S_{Hmax} orientation using our misfit based forward modeling technique. We were, however, able to use borehole breakouts identified in near vertical wellbore sections to constrain the orientations of S_{Hmax} beneath the platform. Two breakouts occurring at depths from 557 - 568 m TVD indicated a circular mean S_{Hmax} orientation of N35.88°W ± 16.1°, and three breakouts occurring at depths from 645-991 m TVD indicated a circular mean S_{Hmax} orientation of N56.76°E ± 24.3°. Additionally, we were able to limit possible stress regimes to either reverse, oblique reverse, or strike-slip, and radial breakouts identified by Wilde and Stock (1997) in deviated platform Holly wellbores not included in our analysis support the presence of a thrust faulting stress regime with A_{ϕ} between 0-1.0.

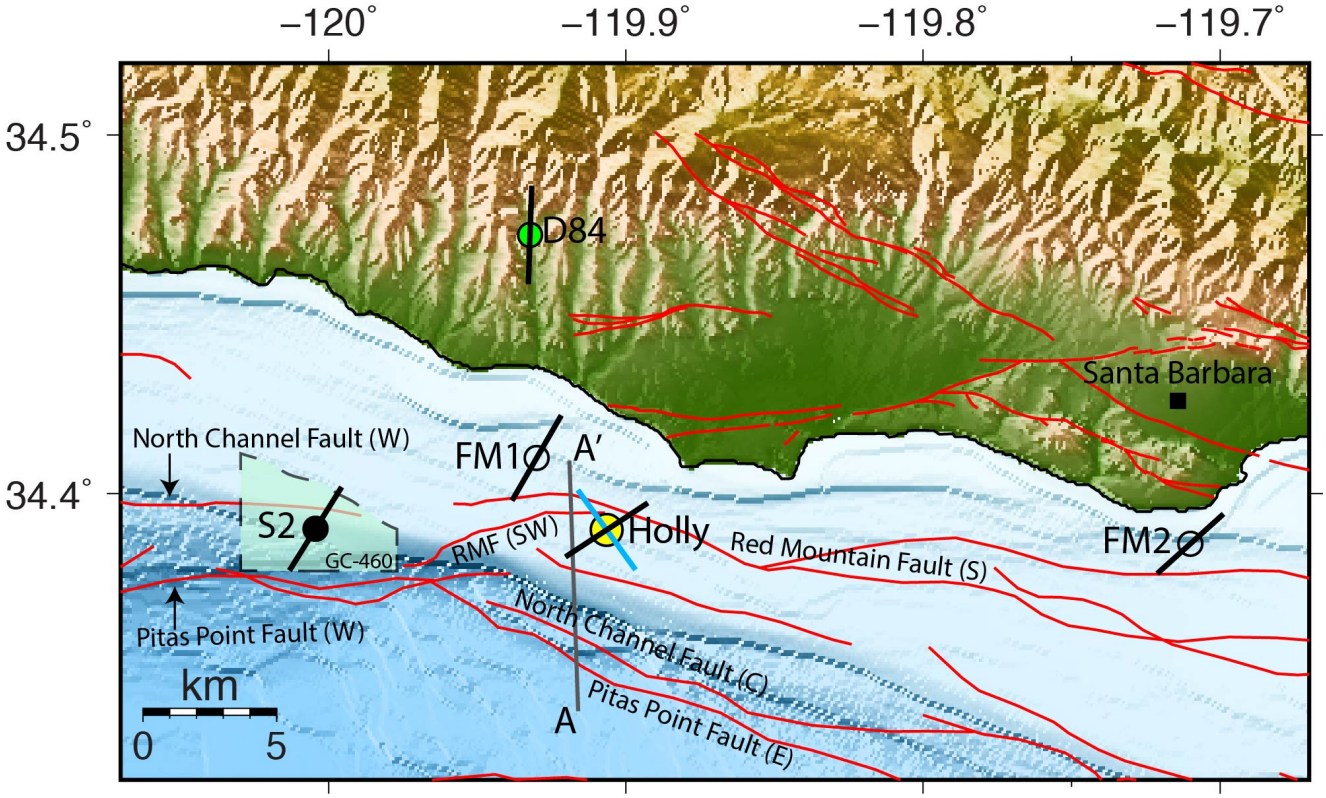

Figure 5.2 Map showing the locations of platform Holly (yellow circle), Heck and Edwards (1998) Samedan #2 well (S2) (black circle) of the Gato Canyon lease 460, Wilde and Stock (1997) Dreyfus #84 well (D84) (green circle), and two single earthquake focal mechanisms from the WSM database (FM1 & FM2) (empty circles), with S_{Hmax} orientations from each stress indicator shown with black lines. The blue line at platform Holly represents S_{Hmax} at 558 - 566 m TVD. FM1 was a M_w 4.9 thrust earthquake that occurred at 8 km depth in 2013, and FM2 was a M_w 5.9 thrust earthquake that occurred at 11.3 km depth in 1978. Regional scale faults are shown in red, and the location of the Gato Canyon 2D seismic profile A-A' is shown with a grey line (See Figure 2.4 for the profile).

Breakouts in near vertical wellbore sections of Well 01 from platform Holly indicate the presence of two distinctly different S_{Hmax} orientations at different depths. At shallow depths, two borehole breakouts indicate an S_{Hmax} orientation of N35.88°W, and at greater depths, three borehole breakouts indicate an S_{Hmax} orientation of N56.76°E (Figure 4.5B). Of the two S_{Hmax} orientations, the

deeper orientation of N56.76°E occurs over a wider depth interval, and is most consistent with previous results from borehole breakouts in the Santa Barbara Channel, and the nearest WSM focal mechanism (FM1) (Figures 1.1A, 5.2). This orientation is therefore taken to possibly represent the dominant S_{Hmax} trend for platform Holly. Thus, the shallower orientation of S_{Hmax} represents a 92.64° counterclockwise rotation of S_{Hmax}. Heck and Edwards (1998) noted a similar rotation of S_{Hmax} in the Samedan #2 well located 10 km west of platform Holly. A preferred fracture strike orientation (parallel to S_{Hmax}) of N55°W in this well was sub-perpindicular to the principal compression direction of N32°E inferred from borehole breakouts, indicating an 87° rotation of S_{Hmax} at certain depths. Additionally, several previous borehole breakout studies have noted similar scale rotations of S_{Hmax} in image logs from individual wellbores. Rajibi et al. (2017) identified a 90° rotation of borehole breakouts over a 4 m interval, Lin et al (2009) identified cases of 90° borehole breakout rotations occurring both abruptly, and gradually over greater borehole lengths, and Shamir and Zoback (1992) observed depth-dependent variations in breakout azimuths from a few degrees to as much as 100° over depth intervals of several centimeters to hundreds of meters. Each of these studies, as well as numerous other studies that also observed various scales of S_{Hmax} rotations occurring with depth in individual wellbores, have attributed these rotations to the presence of faults, fractures, or density contrasts, which cause localized perturbations in the stress field. While tectonic forces contribute significantly to the overall stress state, it is believed that local structures also serve as an important source of stress perturbation (Rajabi et al., 2017). Observations from both Rajibi et al. (2017) and Lin et al. (2010) indicate that abrupt changes of S_{Hmax} are more consistent with the presence of faults, while gradual rotations of S_{Hmax} are more consistent with the presence of fractures. Unfortunately however, there is a 75 m gap in the identified borehole breakouts between the two breakout zones that indicate a N35.88°W S_{Hmax} orientation, and the three that indicate a N56.76°E orientation. Thus, in the absence of borehole televiewer logs, lithological logs, or information on local scale structures near Holly, we are unable to identify the cause of this rotation.

Two prior borehole breakout studies and one WSM earthquake focal mechanism also provide constraints on the orientation of maximum compressive stress in the vicinity of platform Holly (Figure 5.2). In addition to our dominant S_{Hmax} trend of N56.76°E at platform Holly, Heck and Edwards (1998) reported a N32°E orientation of maximum compressive stress at the Samedan #2 well of Gato Canyon lease 460, located roughly 10 km west of platform Holly, Wilde and Stock (1997) constrained a N2°E orientation from the Dreyfus #84 well located onshore, roughly 10 km north of platform Holly, and the WSM database includes a single earthquake focal mechanism (WSM FM1) from a M_w 4.9 thrust faulting earthquake that occurred at 8 km depth just 3.2 km from platform Holly, and indicated a N30°E orientation of S_{Hmax}. We believe that large differences in the orientations of S_{Hmax} in this 10 km x 10 km region that includes platform Holly result not from error, but from heterogeneity in the local stress field due to the structural complexity of the Pitas Point - North Channel - Red Mountain fault system.

Wilde and Stock (1997) identified borehole breakouts in 14 wells in the north channel region near Santa Barbara (See Appendix A14). Of the wellbores that they examined, 13 were highly deviated wells drilled from platform Holly within the Santa Barbara Channel itself. The other, mentioned above, was the Dreyfus #84 well, which is a near-vertical borehole located onshore, roughly 10 km north of platform Holly (Figure 5.2). Wilde and Stock (1997) were unable to confidently constrain a stress regime for their Santa Barbara region data. However, they were able to determine an S_{Hmax} orientation of N2°E from breakouts in the near-vertical Dreyfus #84 well, which they applied to the deviated wellbores from platform Holly. The relatively short distance between the Dreyfus #84 well and platform Holly, however, crosses highly complex structures, and there are several faults of various orientations in this

small area, (Figures 2.3A,B, 2.4, 5,2) most notably those of the Pitas Point – North Channel – Red Mountain fault system. Additionally, breakouts in Dreyfus #84 occurred only at shallow depths between 284 - 558m, while the Wilde and Stock (1997) platform Holly breakouts occurred at depths between 488 - 2790m, and ours occurred at depths between 545 - 1590m. Therefore, while the prior results from the Dreyfus #84 well likely provide an accurate representation of the orientation of maximum compressive stress beneath the onshore location of that well, the breakouts from Well 01 of our dataset likely better represent the orientation of maximum compressive stress beneath platform Holly itself.

Our results, when combined with those of the Samedan #2 well, Dreyfus #84 well, and WSM FM1 show great spatial heterogeneity in the orientations of S_{Hmax} within a 10 km x 10 km area proximate to faults of the Pitas Point – North Channel – Red Mountain fault system (Figures 2.3A,B, 5.2). Within the offshore region along the fault system, we see a 24.76° difference between the S_{Hmax} orientation at platform Holly and the Samedan #2 well located roughly 10 km to the west, and we see a similar 26.76° difference between the S_{Hmax} orientation at platform Holly and WSM FM1 located only 3.2 km to the NE. Furthermore, we see 54.76° difference in the S_{Hmax} orientation between platform Holly and the Dreyfus #84 well, which is located onshore roughly 10 km to the north, and further from the fault system.

Platform Holly, the Samedan #2 well, and WSM FM1 are all located offshore along the Pitas Point - North Channel - Red Mountain fault system, which, as mentioned before, extends 120 km west from the Ventura Basin with few deviations from the general E-W sense of strike (Sorlien and Nicholson, 2015; Sorlien et al., 2016). However, there is a significant boundary near platform Holly at which each of these faults exhibit significant changes in orientation. Beneath the platform, the two deepest faults of this system, the Pitas Point and North Channel faults, show around a 25° clockwise bend in strike, which is accomplished by a geometric segment boundary in the North Channel Fault, and a continuous double bend in strike of the Pitas Point fault (Sorlien et al., 2015; Sorlien and Nicholson, 2015) (Figure 2.3A,B). At this same location, there is also a significant segment boundary and change in strike of the steeply dipping Red Mountain Fault, which is divided into two segments that overlap just west of the platform (Figure 2.3A). The Red Mountain South segment, located mostly east of Holly, strikes nearly E-W, and the Red Mountain SW segment, located just west of platform Holly, strikes NE-SW. Several studies have suggested that a component of left-lateral strike-slip motion is expected along the major faults of the Pitas Point - North Channel - Red Mountain fault system (Sorlien et al., 2015; Sorlien and Nicholson, 2015). Our results, and those from the Samedan #2 well and WSM FM1 are consistent with the complex geometries of and proposed component of left-lateral slip along these faults. The Samedan #2 well is located between two E-W trending segments of the Pitas Point and North Channel faults. The S_{Hmax} orientation of N32°E determined at this well is oriented at a high angle, but not perpendicular to both of these fault segments and is therefore consistent with a component of left-lateral slip along them. WSM FM1 occurred at 8 km depth just 3.2 km NE of platform Holly and is also oriented at a high angle to fault segments at this depth. Finally, a component of left-lateral motion across the 25° clockwise bend in the strike of the Pitas Point and North Channel faults, located near Holly, could potentially induce compressive shortening perpendicular to the NW-trending fault planes, which would be consistent with a local thrust faulting stress regime and N56.76°E orientation of S_{Hmax} that we have constrained.

The proposed components of left-lateral slip along the faults of the Pitas Point - North Channel - Red Mountain fault system may also be consistent with the difference in S_{Hmax} orientations between our

results at platform Holly, WSM FM1, and the Dreyfus #84 well. The S_{Hmax} orientations from platform Holly and WSM FM1, which is located just 3.2 km north of Holly, are N56.76°E and N30°E, respectively. Both of these S_{Hmax} orientations are oriented at a high angle, but not perpendicular, to the nearby faults of the Pitas Point - North Channel - Red Mountain fault system, and are therefore consistent with a component of left-lateral slip. However, the S_{Hmax} orientation of N2°E at the Dreyfus #84 well, which is located onshore, 10 km north of Holly, at a significant distance from offshore fault systems, is oriented nearly perpendicular to the those faults. Thus, the interpreted rotation in the orientation of S_{Hmax} between the offshore and onshore regions could potentially indicate that a transformation to a less oblique and more thrust faulting regime occurs in the 10 km distance north of the faults.

Apparent heterogeneity within the crustal stress field of this region holds significant implications for the debate regarding the seismic hazard potential of the Pitas Point - North Channel - Red Mountain fault system. As mentioned before, Hubbard et al (2014) have linked 6-8 m marine uplift events west of Ventura to paleo-quakes of M_w 7.7 - 8.1, suggesting the possibility of large, multisegment ruptures propagating great lengths along strike of the Pitas Point - North Channel - Red Mountain fault system. However, Sorlien and Nicholson (2015) have suggested that a more complete understanding of the complex offshore fault geometries and segment boundaries in this region, as well as the nature of slip across them would be beneficial to any assessment of the probability of multi-segment earthquakes in this region. Additionally, we have noted that studies of model sensitivity to changes in stress inputs have indicated that increased stress heterogeneity tends to produce shorter rupture lengths (Lozos et al., 2015), and minor rotations to the orientation of maximum compressive stress (30°) can reduce calculated peak ground velocities by up to 40% (Roten et al., 2014). In Well 01 from our dataset alone, we identify a 90° rotation of S_{Hmax}, which shows that there is stress heterogeneity with depth at platform Holly, likely due to fault interactions or fractures. Additionally, our results, when combined with the N2°E S_{Hmax} orientation from Wilde and Stock (1997), the N32°E S_{Hmax} orientation from Heck and Edwards (1998), and the N30°E S_{Hmax} orientation from the WSM FM1 show spatial heterogeneity in S_{Hmax} orientations within a 10 km x 10 km region of high structural complexity in the northern Santa Barbara Channel. Therefore, our results strengthen claims that certain unaccounted for properties of the offshore Pitas Point - North Channel - Red Mountain fault system could potentially prevent rupture from propagating the full length of the fault system and producing a M_w 7.7 - 8.1 earthquake.

CHAPTER 6. CONCLUSIONS

We provide new constraints on crustal stress beneath the Santa Barbara Channel by developing a misfit based forward modeling technique with bootstrap resampling. We also improved borehole breakout selection criteria, and therefore the quality of breakout datasets by developing a new criterion that filters out keyseats. Our new approach is applied to borehole breakout datasets from closely spaced, deviated wells at two locations in the Santa Barbara Channel. Given enough borehole breakouts at a wide range of borehole azimuths and deviations, we are able to confidently constrain the relative magnitudes and orientations of all three principal stress components.

Our constraints at platform Gail indicate the presence of a thrust faulting stress regime with a N45°E orientation of S_{Hmax} (bootstrap confidence range N40°E - N55°E) (Figure 4.3A). These results are consistent with local structures, which reflect deeper regional scale trends, and are also in agreement with previous results in the onshore Oxnard Plain. Despite this consistency in S_{Hmax} orientations, we are cautious about ubiquitously extending Gail's thrust faulting stress regime as far as the onshore region due to prior studies indicating the possibility of a recent strike-slip regime there. Results from platform Holly indicate the presence of a reverse or oblique reverse faulting stress regime with a N56.76°E ± 24.3° orientation of S_{Hmax}. These results, when combined with results from other stress indicators in the offshore region, including a prior borehole breakout study 10 km to the west, and a thrust faulting earthquake focal mechanism 3.2 km to the northwest, which indicated S_{Hmax} orientations of N32°E and N30°E respectively, show significant heterogeneity in the orientation of S_{Hmax} along the Pitas Point - North Channel - Red Mountain fault system. Furthermore, previous borehole breakout studies onshore, roughly 10 km to the north, constrained an S_{Hmax} orientation of N2°E, which indicates a significant heterogeneity in the S_{Hmax} orientation, and potentially the stress regime between the offshore and onshore regions of the northern Santa Barbara Channel. These findings support results from previous studies, which suggest that borehole breakouts are able to record stress on small enough spatial scales to capture short-length scale heterogeneity in the stress field. Thus, we propose that caution be exercised when projecting stress orientations and regimes from borehole breakouts and other spatially sensitive methods into proximate regions.

Similarly, we also propose that care be taken when projecting borehole breakout derived stress constraints across heterogeneous structural domains to depth. Beneath platform Gail, shallow structures are reflective of deeper, regional scale structural trends, giving the impression that stress constraints may be extended to depth. At platform Holly, however, we identified a significant rotation of breakout azimuth occurring in a single well with depth, that is likely due to perturbations in the stress field that may be caused by a fault, fracture, or density contrast. This finding supports previous studies that suggest local structures serve as an important source of stress, and borehole breakouts record stress on a small enough scale to capture stress perturbations that occur locally with depth in individual wellbores (Lin et al., 2010; Rajabi et al., 2017; Shamir and Zoback, 1992).

In light of our results, and those of previous studies, it is not surprising that several studies comparing borehole breakout derived stress constraints and regional focal mechanism stress inversions have identified disagreement between the two. While this disagreement may be in part due to the fact that the two datasets sample different depth intervals of the crust, we offer a further explanation that borehole breakouts are able to resolve stress heterogeneity at a scale that is not matched in focal mechanism inversions. Their sampling of the uppermost crust, where stress is more heterogeneous than

at depth, therefore provides a rich dataset that can be embedded in a regional stress field to better constrain 3D dynamic rupture models of regions with high-risk fault systems like the Santa Barbara Channel.

Dynamic fault rupture models for the northern region of the Santa Barbara channel incorporated regional stress by applying a single, homogeneous stress regime and orientation to the entire fault system being modeled. This practice, however, does not accurately represent the state of stress along active faults, which likely varies substantially, especially at geometric complexities such as step-overs or bends (Liu et al., 2016; Rivera and Kanamori, 2002). Several studies have shown that the assumption of a homogenous stress regime could potentially lead to significant inaccuracies in the results of dynamic rupture and ground motion models, as changes in the orientation of the major principal stress can have a major effect on calculated peak ground velocities (Roten et al., 2014), and increased stress heterogeneity has been shown to produce shorter rupture lengths (Lozos et al., 2015). Thus, dynamic rupture and ground motion models must take stress heterogeneity into account. Our results, when combined with those of similar studies nearby, identify, and provide quantitative constraints on heterogeneity in the regional stress field of the Santa Barbara Channel. If incorporated into dynamic rupture models, such grounded constraints will allow for more precise definition of initial stresses, and therefore contribute to more accurate predictions of rupture scenarios and resulting ground motions.

REFERENCES

Atwater, T., 1970, Implications of Plate Tectonics for the Cenozoic Tectonic Evolution of Western North America: Geological Society of America Bulletin, v. 81, p. 3513-3536.

Atwater, T., and Stock, J., 1998, Pacific-North American Plate Tectonics of the Neogene Southwestern United States: An Update: International Geology Review, v. 40, no. 5, p. 375-402.

Atwater, T. M., 1989, Plate tectonic history of the northeast Pacific and western North America: The Eastern Pacific Ocean and Hawaii, p. 21-72.

Barall, M., and Harris, R. A., 2015, Metrics for Comparing Dynamic Earthquake Rupture Simulations: Seismological Research Letters, v. 86, no. 1, p. 223-235.

Behl, R., Nicholson, C., Sorlien, C., Kennett, J., Marshall, C., Decasari, S. H., and Escobedo, D., 2016, Chronostratigraphy of the Quaternary Santa Barbara Basin: an integrated geophysical, sedimentologic, and paleoceanographic approach: 2016 AAPG Pacific + Rocky Mountain Joint Meeting.

Bell, J. S., 1996, In Situ Stresses in Sedimentary Rocks (Part 2): Applications of Stress Measurements: Geoscience Canada, v. 23, no. 3, p. 135-153.

Bell, J. S., and Gough, D. I., 1979, Northeast-southwest compressive stress in Alberta evidence from oil wells: Earth and Planetary Science Letters, v. 45, no. 2, p. 475-482.

Bent, A. L., and Helmberger, D. V., 1991, Seismic characteristics of earthquakes along the offshore extension of the Western Transverse Ranges, California: Bulletin of the Seismological Society of America, v. 81, no. 2, p. 399-422.

Carminati, E., Scrocca, D., and Doglioni, C., 2010, Compaction-induced stress variations with depth in an active anticline: Northern Apennines, Italy: Journal of Geophysical Research, v. 115, no. B2.

Crouch, J. K., and Suppe, J., 1993, Cenozoic tectonic evolution of the Los Angelas basin and inner California borderland: A model for core complex-like crustal extension: Geological Society of America Bulletin, v. 105, p. 1415-1434.

Day-Lewis, A., Zoback, M., and Hickman, S., 2010, Scale-invariant stress orientations and seismicity rates near the San Andreas Fault: Geophysical Research Letters, v. 37, no. 24, p. n/a-n/a.

Dickinson, W. R., 1996, Kinematics of Transrotational Tectonism in the California Transverse Ranges and Its Contribution to Cumulative Slip Along the San Andreas Transform Fault System: Geol. Soc. Am. Special Paper 305.

DOGGR, 1992, Southern, Central Coastal, and Offshore California Oil and Gas Fields: California Oil and Gas Fields, v. 2, p. 645.

Fairhurst, C., 1967, Methods of determining in-situ rock stresses at great depths, Missouri River Division, US Army, Corps of Engineers.

Fisher, M. A., Greene, H. G., Normark, W. R., and Sliter, R. W., 2005, Neotectonics of the Offshore Oak Ridge Fault near Ventura, Southern California: Bulletin of the Seismological Society of America, v. 95, no. 2, p. 739-744.

Hadley, D., and Kanamori, H., 1977, Seismic Structure of the Transverse Ranges, California: Geological Society of America Bulletin, v. 88, p. 1469 - 1478.

Hardebeck, J., Aagard, B., Becker, T., Shaw, B., and Shaw, J., 2012, SCEC Community Workshop: Community Stress Model.

Hardebeck, J. L., and Hauksson, E., 2001, Crustal stress field in southern California and its implications for fault mechanics: Journal of Geophysical Research: Solid Earth, v. 106, no. B10, p. 21859-21882.

Haukoos, J. S., and Lewis, R. J., 2005, Advanced Statistics: Bootstrapping Confidence Intervals for Statistics with “Difficult” Distributions: ACAD EMERG MED, v. 12, no. 4.

Hauksson, E., Andrews, J., Plesch, A., Shaw, J. H., and Shelly, D. R., 2016, The 2015 Fillmore Earthquake Swarm and Possible Crustal Deformation Mechanisms near the Bottom of the Eastern Ventura Basin, California: Seismological Research Letters, v. 87, no. 4, p. 807-815.

Heck, R. G., and Edwards, E. B., 1998, Gato Canyon Field, Santa Barbara Channel, California: American Association of Petroleum Geologists, p. 293-300.

Heidbach, O., Tingay, M., Barth, A., Reinecker, J., Kurfeß, D., and Müller, B., 2010, Global crustal stress pattern based on the World Stress Map database release 2008: Tectonophysics, v. 482, no. 1-4, p. 3-15.

Hiramatsu, Y., and Oka, Y., 1962, Analysis of stress around a circular shaft or drift excavated in ground in a three dimensional stress state.

Hubbard, J., Shaw, J. H., Dolan, J., Pratt, T. L., McAuliffe, L., and Rockwell, T. K., 2014, Structure and Seismic Hazard of the Ventura Avenue Anticline and Ventura Fault, California: Prospect for Large, Multisegment Ruptures in the Western Transverse Ranges: Bulletin of the Seismological Society of America, v. 104, no. 3, p. 1070-1087.

Ingle, J. C., 1980, Cenozoic paleobathymetry and depositional history of selected sequences within the southern California Continental Borderland: Cushman Foundation Special Publication, v. 19, p. 163-195.

Johnson, S. Y., Hartwell, S. R., Sorlien, C. C., Dartnell, P., and Ritchie, A. C., 2017, Shelf evolution along a transpressive transform margin, Santa Barbara Channel, California: Geosphere, v. 13, no. 6, p. 2041-2077.

Kamerling, M. J., and Luyendyk, B. P., 1985, Paleomagnetism and neogene tectonics of the Northern Channel Islands, California: Journal of Geophysical Research, v. 90, no. B14.

Kerkela, S., and Stock, J. M., 1996, Compression directions north of the San Fernando Valley determined from borehole breakouts: Geophysical Research Letters, v. 23, no. 23, p. 3365-3368.

Larsen, S. C., Agnew, D. C., and Hager, B. H., 1993, Strain accumulation in the Santa Barbara Channel 1970 - 1988: Journal of Geophysical Research, v. 98, no. B2, p. 2119-2133.

Larson, K. M., and Webb, F. H., 1992, Deformation in the Santa Barbara Channel from GPS measurements: Geophysical research Letters, v. 19, no. 14, p. 1491-1494.

Lin, W., Yeh, E.-C., Hung, J.-H., Haimson, B., and Hirono, T., 2010, Localized rotation of principal stress around faults and fractures determined from borehole breakouts in hole B of the Taiwan Chelungpu-fault Drilling Project (TCDP): Tectonophysics, v. 482, no. 1-4, p. 82-91.

Liu, D., Duan, B., and Luo, B., 2016, Stress Heterogeneity at Restraining Double Bends Over Multicycles and Its Effect on Rupture Propagation in 3D: SCEC Annual Meeting 2016.

Lozos, J. C., Oglesby, D. D., Brune, J. N., and Olsen, K. B., 2015, Rupture and Ground-Motion Models on the Northern San Jacinto Fault, Incorporating Realistic Complexity: Bulletin of the Seismological Society of America, v. 105, no. 4, p. 1931-1946.

Luttrell, K. M., and Hardebeck, J. L., 2017, Borehole breakouts versus earthquake focal mechanisms as stress field orientation indicators in southern California: should we agree to disagree: 2017 SCEC Annual Meeting.

Malinverno, A., Saito, S., and Vannucchi, P., 2016, Horizontal principal stress orientation in the Costa Rica Seismogenesis Project (CRISP) transect from borehole breakouts: Geochemistry, Geophysics, Geosystems, v. 17, no. 1, p. 65-77.

Mardia, K. V., and Jupp, P. E., 1972, Directional Statistics, London, Academic Press Inc., Wiley series in probability and statistics.

Marshall, C. J., 2012, Sedimentation in an Active Fold and Thrust Belt from 1Ma to Present, Santa Barbara Channel, California: Cal State Long Beach, 77 p.

Marshall, S., Funning, G., and Owen, S., 2013, Fault slip rates and interseismic deformation in the western Transverse Ranges, California: Journal of Geophysical Research: Solid Earth, v. 118, no. 8, p. 4511-4534.

Mastin, L., 1988, Effect of borehole deviation on breakout orientations: Journal of Geophysical Research, v. 93, no. B8.

Montone, P., Mariucci, M. T., and Pierdominici, S., 2012, The Italian present-day stress map: Geophysical Journal International, v. 189, no. 2, p. 705-716.

Mount, V. S., and Suppe, J., 1992, Present-day stress orientations adjacent to active strike-slip faults: California and Sumatra: Journal of Geophysical Research, v. 97, no. B8.

Nicholson, C., 2017, Continuing to Evaluate 3D Fault Geometry in Special Fault Study Areas and to Update & Improve the SCEC Community Fault Model: 2016 SCEC Annual Report, v. 16065, p. 8 pp.

Nicholson, C., Sorlien, C. C., Atwater, T., Crowell, J. C., and Luyendyk, B. P., 1994, Microplate capture, rotation of the western transverse ranges, and initiation of the San Andreas transform as a low angle fault system: Geology, v. 22, p. 491 - 495.

Parker, R. L., and McNutt, M. K., 1980, Statistics for the One-Norm Misfit Measure: Journal of Geophysical Research Atmospheres, v. 85, p. 4429-4430.

Peška, P., and Zoback, M. D., 1995, Compressive and tensile failure of inclined well bores and determination of in situ stress and rock strength: Journal of Geophysical Research: Solid Earth, v. 100, no. B7, p. 12791-12811.

Pinter, N., Sorlien, C. C., and Scott, A., 1998, Late Quaternary faulting and folding on Santa Cruz Island, California: Weigland P., ed, Contributions to the Geology of the Northern Channel Islands: Pacific Section, American Association of Petroleum Geologists, p. 111-122.

Plumb, R. A., and Hickman, S. H., 1985, Stress-induced borehole elongation: A comparison between the four-arm dipmeter and the borehole televiewer in the Auburn Geothermal Well: Journal of Geophysical Research: Solid Earth, v. 90, no. B7, p. 5513-5521.

Qian, W., and Pedersen, L. B., 1991, Inversion of borehole breakout orientation data: Journal of Geophysical Research: Solid Earth, v. 96, no. B12, p. 20093-20107.

Rajabi, M., Tingay, M., King, R., and Heidbach, O., 2017, Present-day stress orientation in the Clarence-Moreton Basin of New South Wales, Australia: a new high density dataset reveals local stress rotations: Basin Research, v. 29, p. 622-640.

Reinecker, J., Tingay, M., and Muller, B., 2003, Borehole breakout analysis from four-arm caliper logs: World Stress Map Project.

Rivera, L., and Kanamori, H., 2002, Spatial heterogeneity of tectonic stress and friction in the crust: Geophysical Research Letters, v. 29, no. 6.

Rockwell, T., Wilson, K., Gamble, L., Oskin, M., and Haaker, E., 2014, Great earthquakes in the western Transverse Ranges of southern California on the Pitas Point-Ventura thrust system: 5th International INQUA Meeting on Paleoseismology, Active Tectonics and Archeoseismology (PATA).

Roten, D., Olsen, K. B., Day, S. M., Cui, Y., and Fäh, D., 2014, Expected seismic shaking in Los Angeles reduced by San Andreas fault zone plasticity: Geophysical Research Letters, v. 41, no. 8, p. 2769-2777.

Ryan, K. J., Geist, E. L., Barall, M., and Oglesby, D. G., 2015, Dynamic models of an earthquake and tsunami offshore Ventura, California: Geophysical Research Letters, v. 42, no. 6599 - 6606.

Sankur, V., Weber, L. S., and Masoner, L. O., 1990, Development of Sockeye Field in Offshore California: A Case History: Society of Petroleum Engineers, v. SPE 20047, p. 305-315.

Seeber, L., and Sorlien, C. C., 2000, Listric Thrusts in the Western Transverse Ranges, California: GSA Bulletin, v. 112, no. 7, p. 1067-1079.

Shamir, G., and Zoback, M. D., 1992, Stress orientation profile to 3.5 km depth near the San Andreas Fault at Cajon Pass, California: Journal of Geophysical Research, v. 97, no. B4.

Shaw, J. H., and Suppe, J., 1994, Active Faulting and Growth Folding in the Eastern Santa Barbara Channel, California: Geological Society of America Bulletin, v. 106, p. 607-626.

Sibson, R. H., 2004, Frictional Mechanics of Seismogenic Thrust Systems in the Upper Continental Crust - Implications for Fluid Overpressures and Redistribution: AAPG Memoir, v. 82, p. 1-17.

Snee, J.-E. L., and Zoback, M., 2018, State of stress in the Permian Basin, Texas and New Mexico: Implications for induced seismicity: The Leading Edge, Special Section: Induced Seismicity, p. 810-818.

Sorlien, C. C., Bennett, J. T., Cormier, M.-H., Campbell, B. A., Nicholson, C., and Bauer, R. L., 2015, Late Miocene–Quaternary fault evolution and interaction in the southern California Inner Continental Borderland: Geosphere, v. 11, no. 4, p. 1111-1132.

Sorlien, C. C., and Kamerling, M. J., 2000, Fault displacement and fold contraction etimated by unfolding Quaternary strata, onshore and offshore Ventura basin, California: USGS Technical Report.

Sorlien, C. C., and Nicholson, C., 2015, Post-1 Ma Deformation History of the Pitas Point-North Channel-Red Mountain Fault System and Associated Folds in Santa Barbara Channel, California.

Sorlien, C. C., Nicholson, C., Behl, R. J., and Kamerling, M. J., 2016, Displacement Direction and 3D Geometry for the South-Directed North Channel - Pitas Point Fault System and North-Directed Ramps, Decollements, and Other Faults Beneath Santa Barbara Channel: SCEC Annual Meeting 2016.

Vedder, J. G., Wagner, H. C., and Schoellhamer, J. E., 1969, Geologic Framework of the Santa Barbara Channel Region: Geological Survey Professional Paper, v. 679-A, p. 1-11.

Vernik, L., and Zoback, M. D., 1992, Estimation of Maximum Horizontal Principal Stress Magnitude from Stress-Induced Well Bore Breakouts in the Cajon Pass Scientific Research Borehole: Journal of Geophysical Research, v. 97, no. B4, p. 5109-5119.

Wallace, T. C., Helmberger, D. V., and Ebel, J. E., 1981, A broadband study of the 13 August 1978 Santa Barbara Earthquake: Bulletin of the Seismological Society of America, v. 71, no. 6, p. 1701-1718.

Wilde, M., and Stock, J., 1997, Compression directions in southern California (from Santa Barbara to Los Angeles Basin) obtained from borehole breakouts: Journal of Geophysical Research: Solid Earth, v. 102, no. B3, p. 4969-4983.

Yang, W., and Hauksson, E., 2013, The tectonic crustal stress field and style of faulting along the Pacific North America Plate boundary in Southern California: Geophysical Journal International, v. 194, no. 1, p. 100-117.

Yeats, R. S., 1976, Neogene Tectonics of the Central Ventura Basin, California: The Neogene Symposium, p. 19 - 32.

Yeats, R. S., Huftile, G. J., and Grigsby, F. B., 1988, Oak Ridge fault, Ventura fold, and the Sisar decollement: Geology, v. 16, p. 1112-1116.

Zajac, B., 1997, The State of Stress as Inferred From deviated boreholes: Constraints on the tectonics of offshore central california and cook inlet, Alaska: Caltech, 298 p.

Zoback, M. D., 2007, Reservoir Geomechanics.

Zoback, M. D., Barton, C. A., Brudy, M., Castillo, D. A., Finkbeiner, T., Grollimund, B. R., Moos, D. B., Peska, P., Ward, C. D., and Wiprut, D. J., 2003, Determination of stress orientation and magnitude in deep wells: International Journal of Rock Mechanics and Mining Sciences, v. 40, no. 7-8, p. 1049-1076.

Zoback, M. L., 1992, First- and second-order patterns of stress in the lithosphere: The World Stress Map Project: Journal of Geophysical Research, v. 97, no. B8.

APPENDIX. SUPPLEMENTARY MATERIALS

A1. Log data used in the interpretation of borehole breakouts

Six individual log measurements from oriented 4-arm caliper tools are needed for the interpretation of borehole breakouts (Reinecker et al., 2003). These six logs are:

1. Caliper lengths (C1 & C2): Two caliper arms record the diameter of the borehole at orthogonal axes. Caliper 1 (C1) measures the diameter between pads 1 and 3 and 'Caliper 2' (C2) measures the diameter between pads 2 and 4;

2. Azimuth of pad 1 (P1AZ): Pad 1 on the tool serves as the "reference pad", and its azimuth is magnetically recorded with respect to the magnetic north (Plumb and Hickman, 1985)

3. Borehole deviation (DEVI): The angle of borehole dip from the vertical Z axis.

4. Azimuth of borehole drift (HAZI): Measures the azimuth of borehole drift away from the well pad in the XY plane of the geographical reference frame.

5. Relative bearing of pad 1 (RB): Records the angle θ of pad1 from the J axis (high side of hole) in the borehole coordinate system.

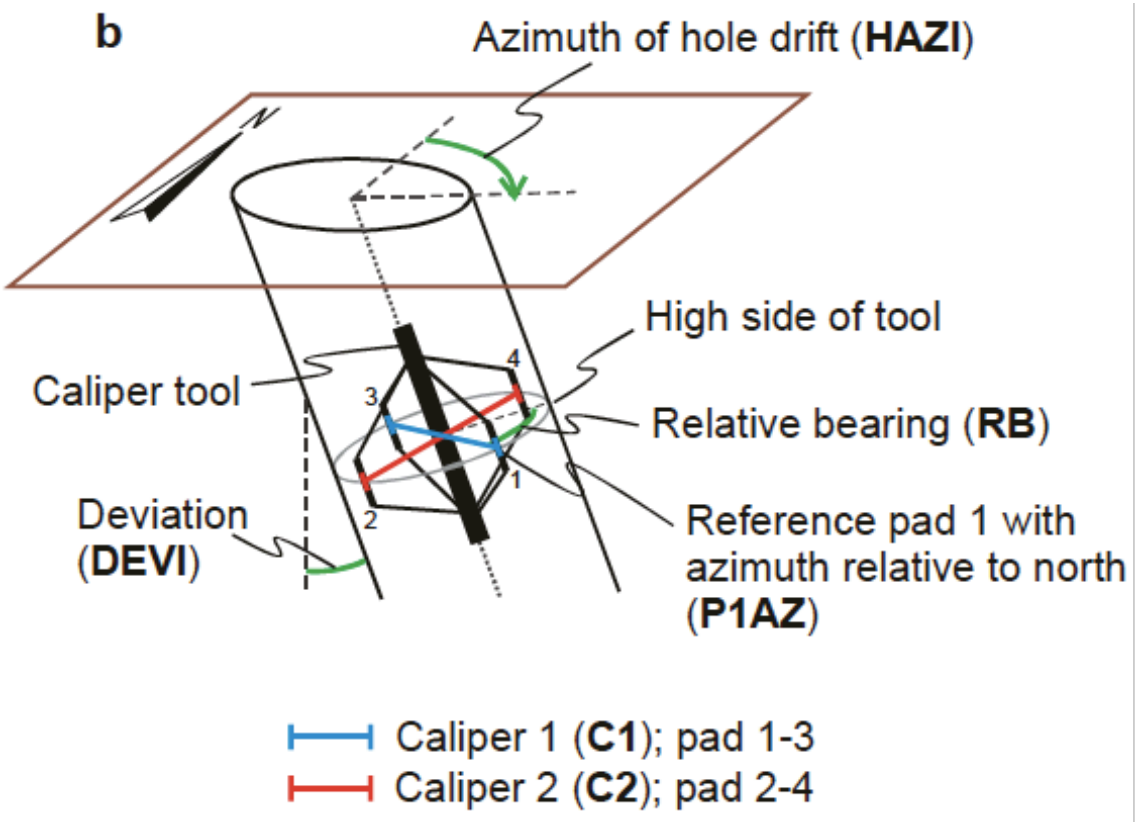

Figure A 1. Diagram from Reinecker et al. (2003) showing the geometry of the 4-arm caliper tool in the borehole, and data used for interpreting borehole breakouts.

A2. Polar plots of borehole breakout orientations

In order to view borehole breakout results and compare them to theoretical breakout orientations, breakouts are plotted on a polar projection using the "looking down the borehole" convention of Peska and Zoback (1995). Using this convention, each borehole breakout is plotted as a single tick mark which represents the borehole azimuth and deviation at which the breakout occurred, and the elongation orientation of the breakout (RB). Each of these values are represented as follows:

Borehole azimuth at breakout location (HAZI) - Represented by the location of the tick mark radially about the center of the plot. Values increase in a clockwise direction from the top of the plot such that 0°/360° = north, 90° = east, 180° = south, 270° = west.

Borehole deviation from vertical at breakout location (DEVI) - Represented by the distance of the tick mark from the center of the plot. Breakouts occurring in vertical boreholes (0°) are plotted at the center of the plot, while horizontal breakouts (90°+) are plotted on the periphery.

Breakout elongation orientation - Using the "looking down the borehole" convention, the elongation orientation of the breakout (RB) is plotted as the angle between the tick mark and the radius of the plot that the tick mark is plotted on (determined by borehole azimuth). A breakout with RB = 0° will plot parallel to this radius (radially), and increasing values rotate the tick mark clockwise.

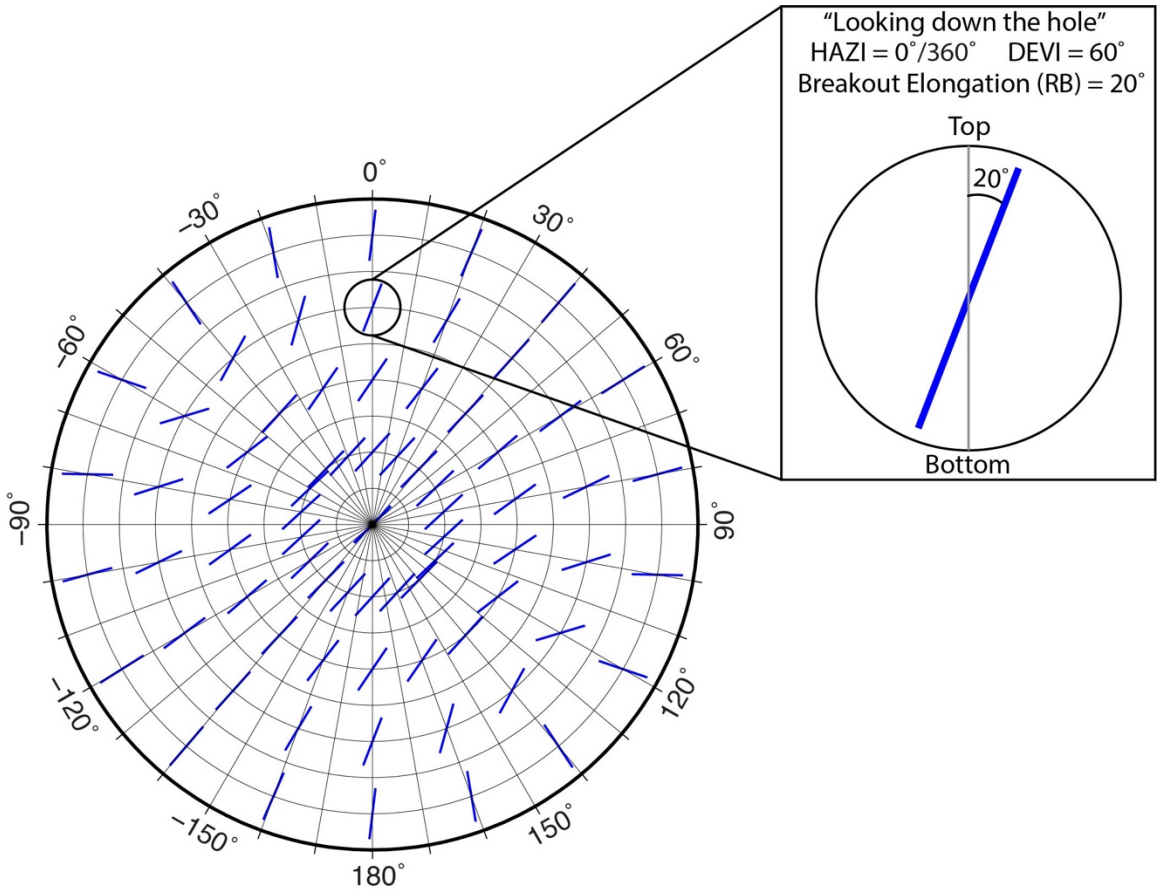

Figure A 2. Diagram based on Zoback (2007) showing the "looking-down-the-well" convention of plotting borehole breakout orientations on a polar projection.

A3. Theoretical breakout patterns

The position at which borehole breakouts form in non-vertical boreholes is dependent on the orientations and relative magnitudes of all three principal stress components, as well as the orientation of the wellbore itself (e.g. Qian and Pedersen, 1991). In an unchanging stress regime, the position at which borehole breakouts form varies systematically as wellbore orientation changes. This systematic variation in breakout orientation as wellbore orientation changes is shown for various stress regimes with A_ϕ ranging from 0 to 3.0 in Figure A3.

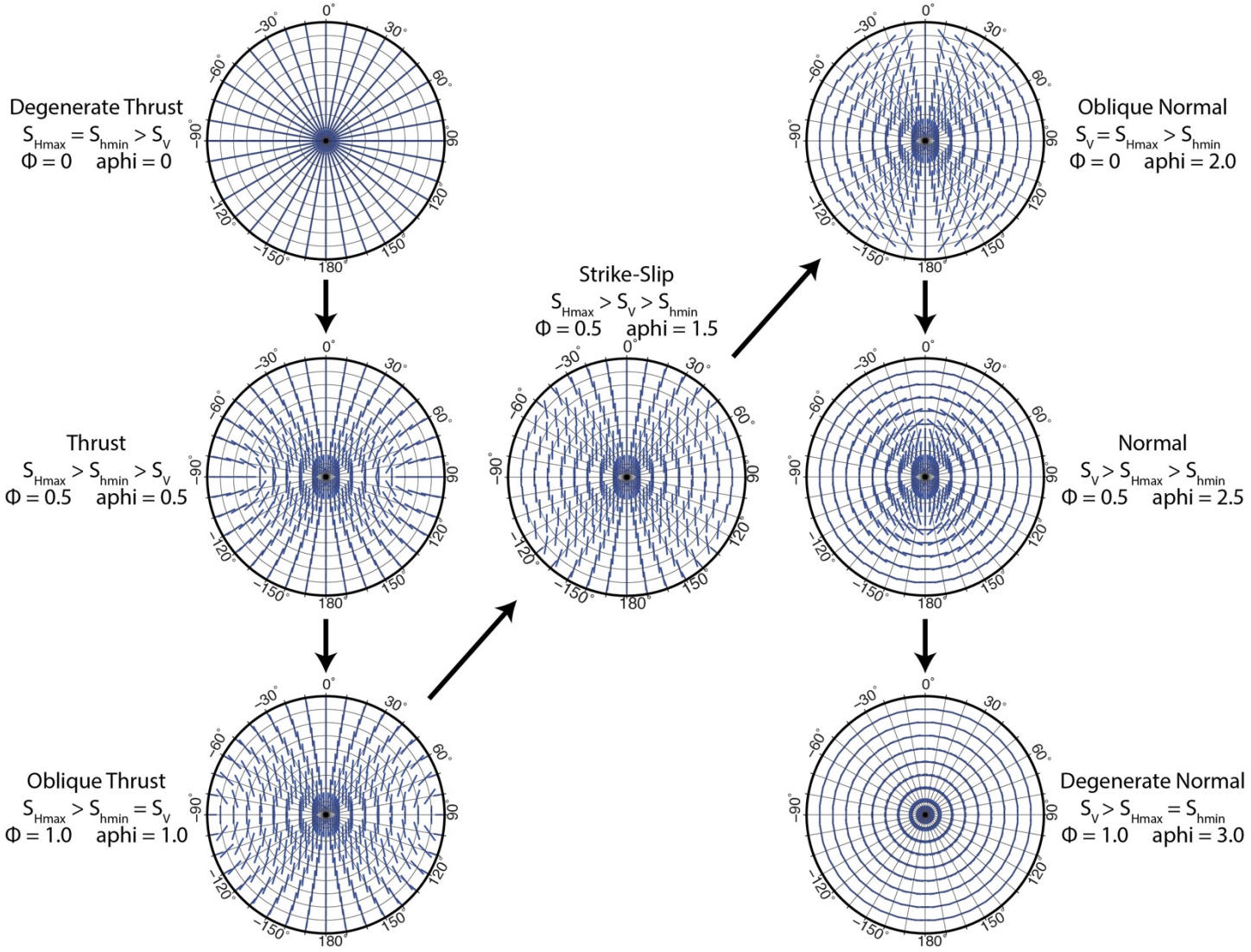

Figure A 3. Polar plots showing theoretical breakout patterns of borehole breakouts for a variety of borehole orientations and stress regimes

A4. Averaging borehole breakout data

4-arm caliper data in this study are recorded as discrete data points at 0.5 ft (0.1524 m) logging increments. Once all breakout criteria are met, we determine a mean depth value, as well as circular mean values for the breakout elongation orientation, borehole azimuth, and borehole deviation such that each separate breakout zone can be defined by a single value of each. Statistical techniques appropriate for linear data are not always appropriate for circular or angular data, as two orientations of 1° and 360° would yield an average orientation of 180°. Thus, in order to obtain the mean of azimuthal values, we use circular mean equations from Mardia and Jupp (1972):

Given unit vectors $x_1,\ldots..x_n$ with corresponding angles $\theta_1 \ldots\ldots \theta_n$, the cartesian coordinates of x_j are $(cos\theta_j, sin\theta_j)$, and the cartesian coordinates of the mean orientation are $(\bar{C}, \bar{S})$ such that:

$$\bar{C} = \frac{1}{n}\sum_{j=1}^{n} cos\ \theta_j$$

$$\bar{S} = \frac{1}{n}\sum_{j=1}^{n} sin\ \theta_j$$

The mean orientation is obtained using the equation:

$$\bar{\theta} = \begin{cases} tan^{-1}\ (\bar{S}/\bar{C}) & if\ \bar{C} \geq 0 \\ tan^{-1}\ (\bar{S}/\bar{C}) + \pi & if\ \bar{C} \geq 0 \end{cases}$$

Averaging breakout data points reduces computation time by reducing the amount of borehole breakout data points for which theoretical borehole breakout orientations must be calculated. At platform Gail, averaging breakouts reduced the number of theoretical breakout orientations to be calculated per forward model from 7571 to 148, and at platform Holly, averaging borehole breakouts reduced the number of theoretical breakout orientations to be calculated per forward model from 3394 to 89.

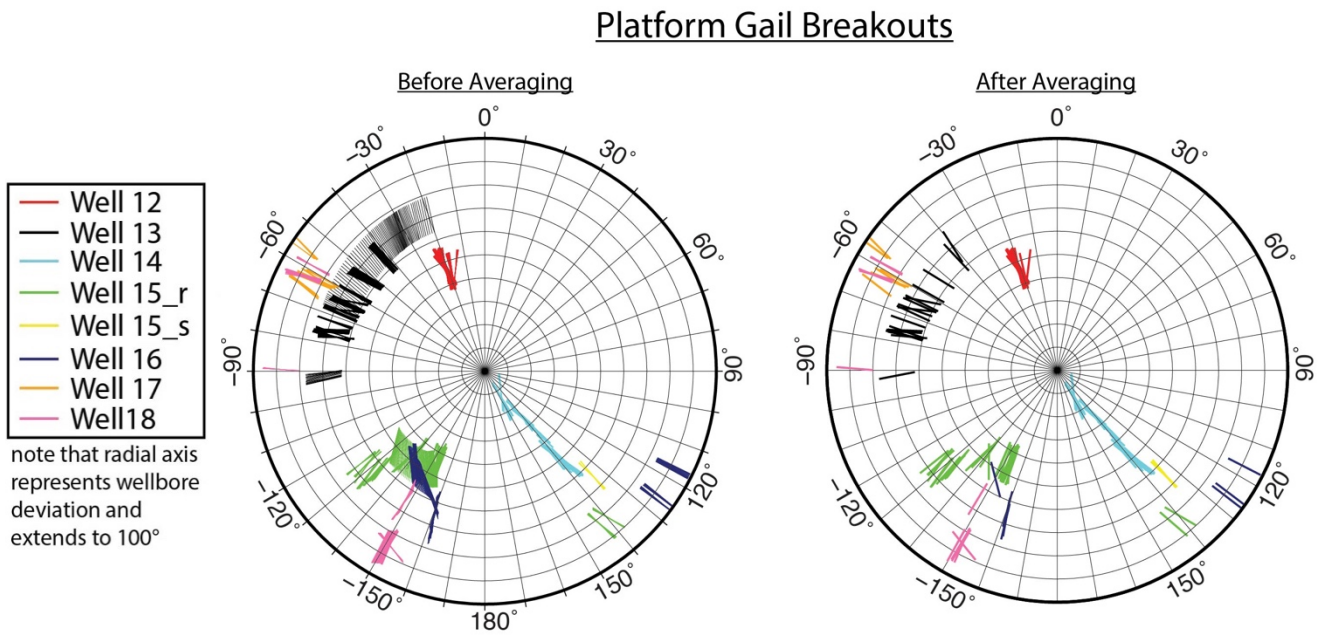

Figure A 4. Polar plots of platform Gail breakouts before and after circular mean values for breakout elongation orientation, borehole azimuth, and borehole deviation are calculated such that each separate breakout zone can be defined by a single value of each.

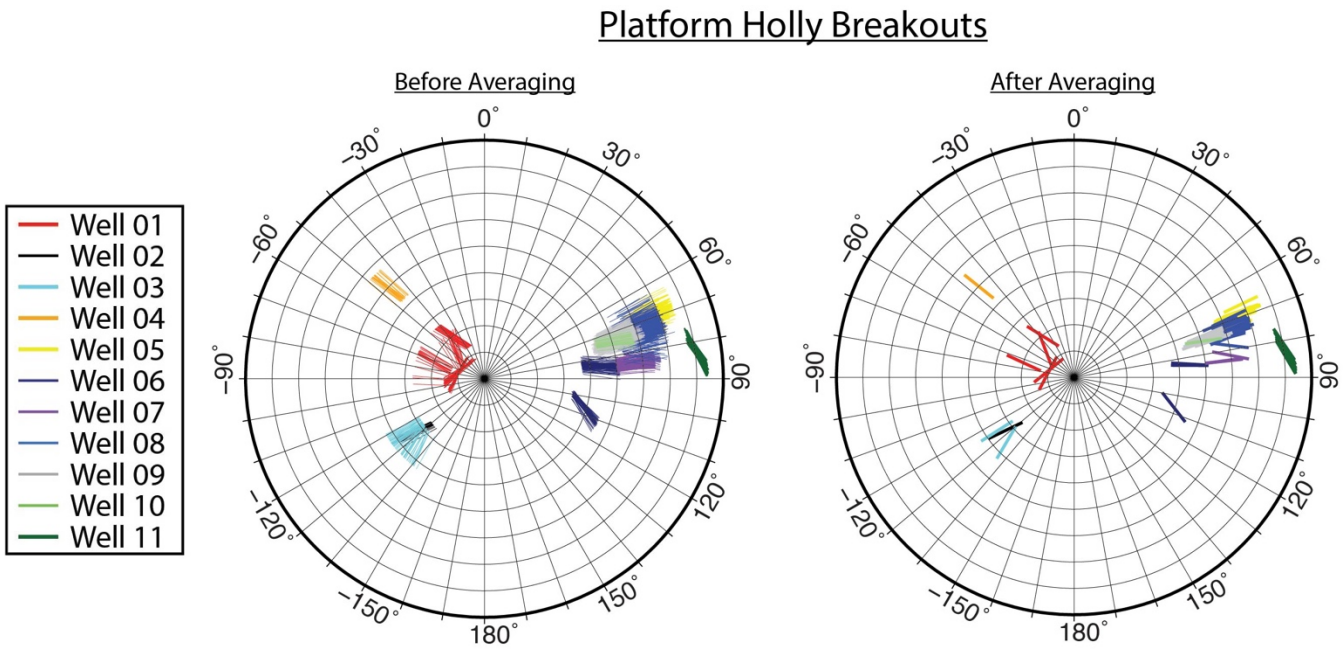

Figure A 5. Polar plots of platform Holly breakouts before and after circular mean values for breakout elongation orientation, borehole azimuth, and borehole deviation are calculated such that each separate breakout zone can be defined by a single value of each.

A5. Euler angle (α) rotation of the stress state

Operating under the assumption of a vertical principal stress restricts rotation of the stress tensor to a single degree of freedom about the vertical, or z-axis. This rotation is represented by the Euler angle (α) which describes the clockwise rotation from north of S_{hmin} (90° from S_{Hmax}) about the vertical, or z-axis in the horizontal plane. The effect of the Euler angle, α, rotation on theoretical breakout orientations at arbitrary wellbore orientations is show in Figure A6.

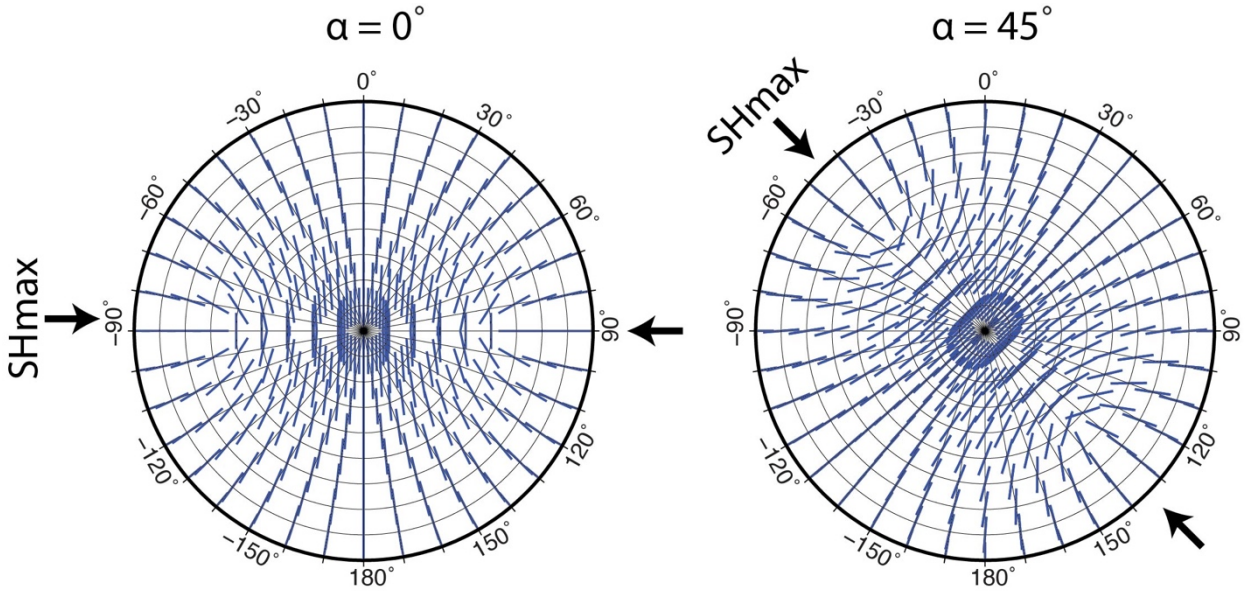

Figure A 6. Effect of a Euler angle α rotation of 45° on theoretical breakout orientations. The entire theoretical plot is rotated about the Z-axis as the horizontal principal stress directions are rotated.

A6. Principal stress tensor and rotation into the borehole coordinate system

In arbitrarily oriented wellbores, the position of maximum compressive stress at the wellbore wall is dependent on the relative magnitudes and orientations of the principal stresses as well the orientation of the well with respect to the stress field (Zoback, 2007). Therefore, in order to calculate the theoretical orientations at which borehole breakouts in arbitrarily oriented boreholes for a given stress regime will form, we must first rotate the principal stress tensor into the geographic coordinate system (XYZ) using the Euler angles α, β, and γ, which describe three successive rotations of the stress tensor about various axes to completely describe its orientation. Then we must rotate the resulting geographically oriented stress tensor into the borehole coordinate system using the azimuth (δ) and deviation (ϕ) of the arbitrarily oriented borehole (Zoback, 2007).

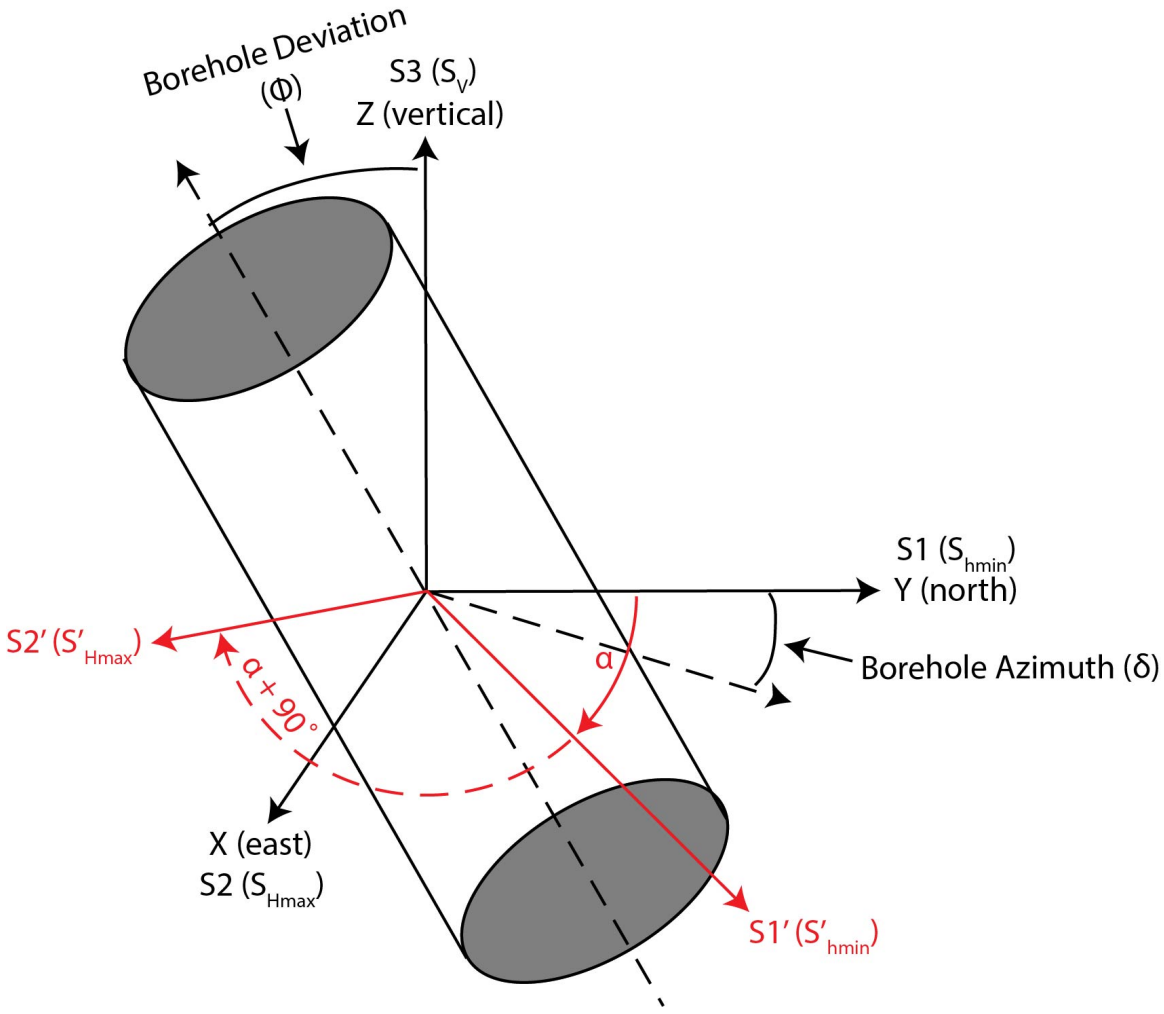

Figure A 7 Schematic diagram based on Zajac (1997) showing the orientations of S_{hmin}, S_{Hmax}, and S_V before and after Z axis rotation by Euler angle (α). Diagram also shows the geometry of borehole azimuth (δ) and deviation (ϕ) which are used to rotate the stress tensor into the borehole coordinate system.

The principal stresses in tensor notation are defined as:

$$S_s = \begin{Bmatrix} S1 & 0 & 0 \\ 0 & S2 & 0 \\ 0 & 0 & S3 \end{Bmatrix}$$

Where S1 ≥ S2 ≥ S3, with pre Euler angle rotation orientations shown in Figure A7.

However, operating under the assumption of a vertical principal stress restricts rotation of the principal stress tensor to a single degree of freedom about the Z-axis, and as such, we must define the stress tensor using S_{hmin}, S_{Hmax}, and S_V with pre Euler angle rotation orientations shown in Figure A8. The new principal stress tensor is therefore defined as:

$$S_s = \begin{Bmatrix} S_{hmin} & 0 & 0 \\ 0 & S_{Hmax} & 0 \\ 0 & 0 & S_V \end{Bmatrix}$$

In calculating theoretical borehole breakout orientations for forward modeled stress states, he values of S_{hmin}, S_{Hmax}, and S_V are populated by the 715 relative magnitude combinations of the principal stresses.

Rotation into the geographic coordinate system using the Euler angles α, β, and γ is performed using the rotation matrix R_s defined by Zoback (2007) as

$$R_s = \begin{Bmatrix} cos\,a\,cos\,\beta & sin\,a\,cos\,\beta & -sin\,\beta \\ cos\,a\,sin\,\beta\,sin\,\gamma - sin\,\alpha\,cos\,\gamma & sin\,\alpha\,sin\,\beta\,sin\,\gamma + cos\,\alpha\,cos\,\gamma & cos\,\beta\,sin\,\gamma \\ cos\,\alpha\,sin\,\beta\,cos\,\gamma + sin\,\alpha\,sin\,\gamma & sin\,\alpha\,sin\,\beta\,cos\,\gamma - cos\,a\,sin\,\gamma & cos\,\beta\,cos\,\gamma \end{Bmatrix}$$

As mentioned above, when operating under the assumption of a vertical principal stress rotation of the principal stress tensor is restricted to a single degree of freedom about the Z-axis. Thus, throughout this study only Euler angle α is allowed to vary (1° - 180°), and Euler angles β, and γ are constantly set to 0°.

Rotation of the stress tensor into the borehole coordinate system using borehole azimuth (δ) and deviation (ϕ) of the arbitrarily oriented borehole is performed using the rotation matrix R_b defined by Zoback (2007) as:

$$R_b = \begin{Bmatrix} -cos\,\delta\,cos\,\phi & -sin\,\delta\,cos\,\phi & sin\,\phi \\ sin\,\delta & -cos\,\delta & 0 \\ cos\,\delta\,sin\,\phi & sin\,\delta\,sin\,\phi & cos\,\phi \end{Bmatrix}$$

In this study, we calculate theoretical borehole breakout orientations using the borehole orientations (hole azimuth and deviation) at which observed borehole breakouts occurred.

With the rotation matrices R_s and R_b defined, the complete stress tensor can be expressed in the borehole coordinate system using the equation defined by Zoback (2007) as:

$$S = R_b R_s' S_s R_s R_b'$$

The tensor of the arbitrary stress field that has been rotated into the borehole coordinate system associated with the arbitrarily oriented borehole is defined by Zoback (2007) as

$$S = \begin{Bmatrix} \sigma_{11} & \sigma_{12} & \sigma_{13} \\ \sigma_{21} & \sigma_{22} & \sigma_{23} \\ \sigma_{31} & \sigma_{32} & \sigma_{33} \end{Bmatrix}$$

A7. Calculation of theoretical breakout orientations

Once the arbitrary stress field has been rotated into the borehole coordinate system of the arbitrarily oriented borehole, equations derived by Hiramatsu and Oka (1962) and Fairhurst (1968) are used to calculate the individual effective stress components around the wellbore. σ_{zz} is stress along the wellbore axis, $\sigma_{\theta\theta}$ is hoop stress, $\tau_{\theta z}$ is shear stress, and σ_{rr} is radial stress. The equations for the individual effective stress components as presented in Zoback (2007) are:

$$\sigma_{zz} = \sigma_{33} - 2\nu(\sigma_{11} - \sigma_{22})cos2\theta - 4\nu\sigma_{12}sin2\theta$$

$$\sigma_{\theta\theta} = \sigma_{11} + \sigma_{22} - 2(\sigma_{11} - \sigma_{22})cos2\theta - 4\nu\sigma_{12}sin2\theta - \Delta P$$

$$\tau_{\theta z} = 2(\sigma_{23}cos\theta - \sigma_{13}sin\theta)$$

$$\sigma_{rr} = \Delta P$$

Where ν is Poisson's ratio, which is set to 0.25 throughout this study, ΔP is the difference between borehole fluid pressure and the in-situ pore pressure, which is set to 0 throughout this study, and θ is the angle around the wellbore measured clockwise from the top of the borehole. We calculate effective stress values at all angles around the borehole such that θ varies from 0.1° - 360° in increments of 0.1°.

We then calculate the minimum and maximum principal effective stresses (σ_{tmax} and σ_{tmin}) for all angles around the wellbore wall (θ) using the following equations, and the angle (θ) at which σ_{tmax} is maximized is selected at the theoretical borehole breakout orientation for the given stress regime (S_{Hmax}, S_{hmin}, S_V), S_{Hmax} orientation (α+90°), and borehole orientation (azimuth (δ) and deviation (ϕ)).

$$\sigma_{tmax} = \frac{1}{2}(\sigma_{zz} + \sigma_{\theta\theta} + \sqrt{(\sigma_{zz} - \sigma_{\theta\theta})^2 + 4\boldsymbol{\tau_{\theta z}^2}})$$

$$\sigma_{tmin} = \frac{1}{2}(\sigma_{zz} + \sigma_{\theta\theta} - \sqrt{(\sigma_{zz} - \sigma_{\theta\theta})^2 + 4\boldsymbol{\tau_{\theta z}^2}})$$

A8. Bootstrapping

In statistics, bootstrapping is any test or metric that relies on random sampling with replacement (Table A1). To ensure confidence in our forward modeling misfit calculation, we randomly resample our original set of observed borehole breakouts 100 times, and compute the best-fit stress regime and S_{Hmax} orientation of each. Once the best-fit stress regimes and S_{Hmax} orientations from each of the 100 bootstrap datasets have been selected, we compile the results and calculate the median value of each. The median is used because it is a more valid summary statistic for non-normally distributed data than the mean (Haukoos and Lewis, 2005).

Table A 1. Example of bootstrap resampling

ORIGINAL	BOOTSTRAP 1	BOOTSTRAP 2	BOOTSTRAP 3	BOOTSTRAP 4	BOOTSTRAP 5
1	**5**	**7**	**4**	**8**	**9**
2	**5**	**1**	**2**	**4**	**5**
3	**4**	**6**	**6**	**7**	**9**
4	**8**	**6**	**3**	**8**	**4**
5	**7**	**9**	**1**	**5**	**8**
6	**8**	**5**	**8**	**1**	**4**
7	**10**	**4**	**3**	**4**	**9**
8	**10**	**7**	**5**	**5**	**8**
9	**2**	**8**	**7**	**3**	**4**
10	**2**	**6**	**4**	**2**	**3**

A9. Gaps in stress ratio (ϕ) values represented in misfit plots

To represent a full range of possible stress regimes, we allow the magnitude of each principal stress component to vary from 1.0 - 2.0 in increments of 0.1 such that there are 11 possible values for each. We then determine all unique numerical combinations of the three principal stress values, excluding those that are either illogical ($S_{Hmax} > S_{hmin}$) or unrealistic ($S_{Hmax} = S_{hmin} = S_V$), and are left with 715 unique principal stress magnitude combinations that represent a range of normal, oblique normal, strike-slip, oblique reverse, and reverse faulting stress regimes.

We define the stress ratio (ϕ) as:

$$\phi = \frac{S_1 - S_2}{S_1 - S_3}$$

While each of the 715 principal stress magnitude combinations do represent a unique numerical combination of S_{Hmax}, S_{hmin}, and S_V, these numerical combinations only give 33 unique values of the stress ratio (ϕ). This is because there are only 11 possible values that each of the principal stress magnitude values can inherit (3 x 11 = 33). Thus, in the stress ratio range of 0 - 1.0, only 33 values are represented, and there are gaps between these values which represent stress ratios that can not be achieved by any combination of the given numerical values (Figure. A8).

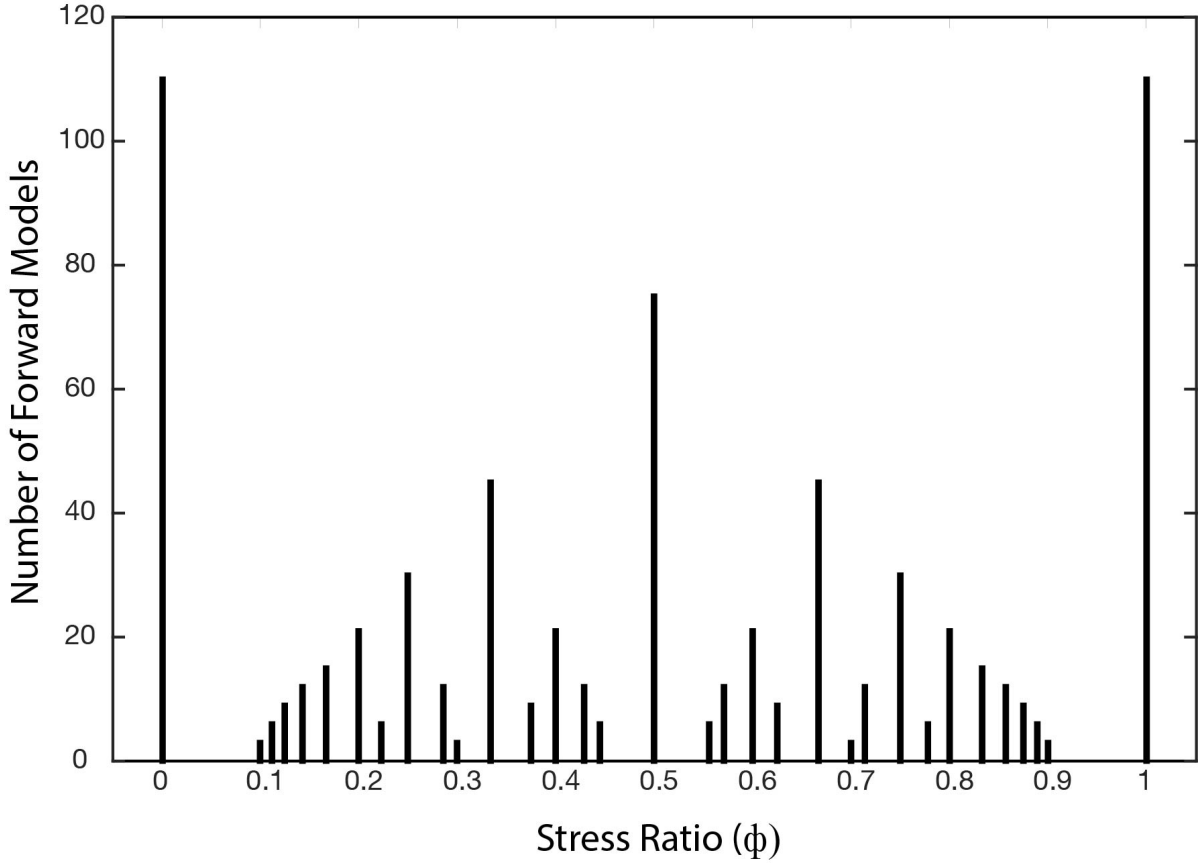

Figure A 8 Histogram showing the distribution of stress ratios for the 715 relative magnitude combinations of S_{Hmax}, S_{hmin}, and S_V. Gaps between the 33 possible stress ratio values represent stress ratios that can not be obtained by any combinations of the three principal stress values given that each are constrained to 11 possible values ranging from 0 - 1.0.

A10. Platform Gail data coverage

We analyzed eight deviated wells from platform Gail where recorded depths ranged from 790 – 1770 m TVD (true vertical depth). Depths of recorded 4-arm caliper data are shown in Figure A9, and all borehole orientations at which data were logged are shown in Figure A10.

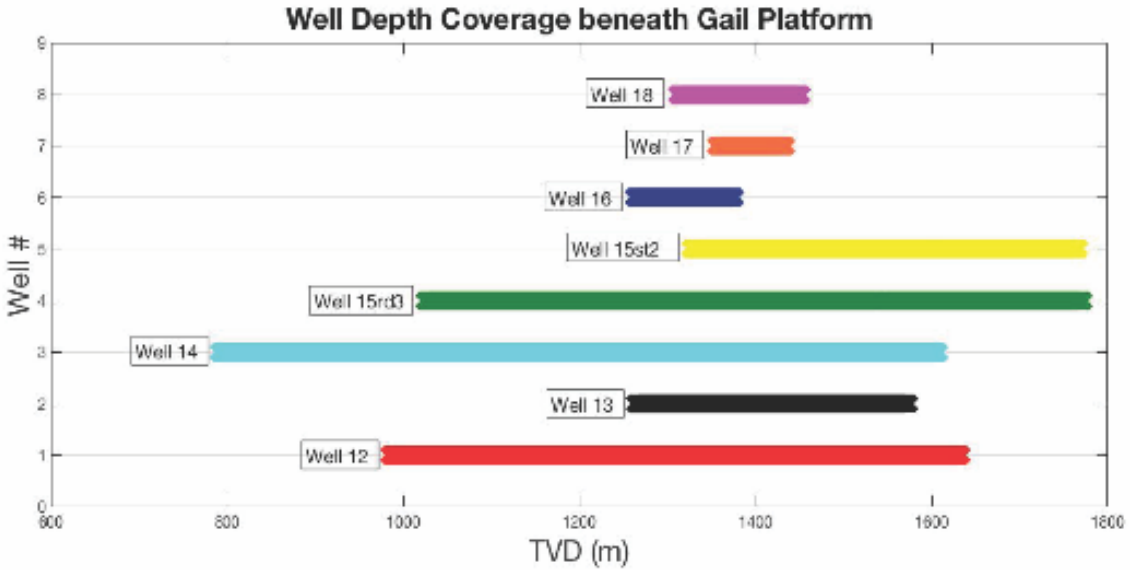

Figure A 9. Graph of borehole depths (TVD - m) at which 4-arm caliper data were logged at platform Gail

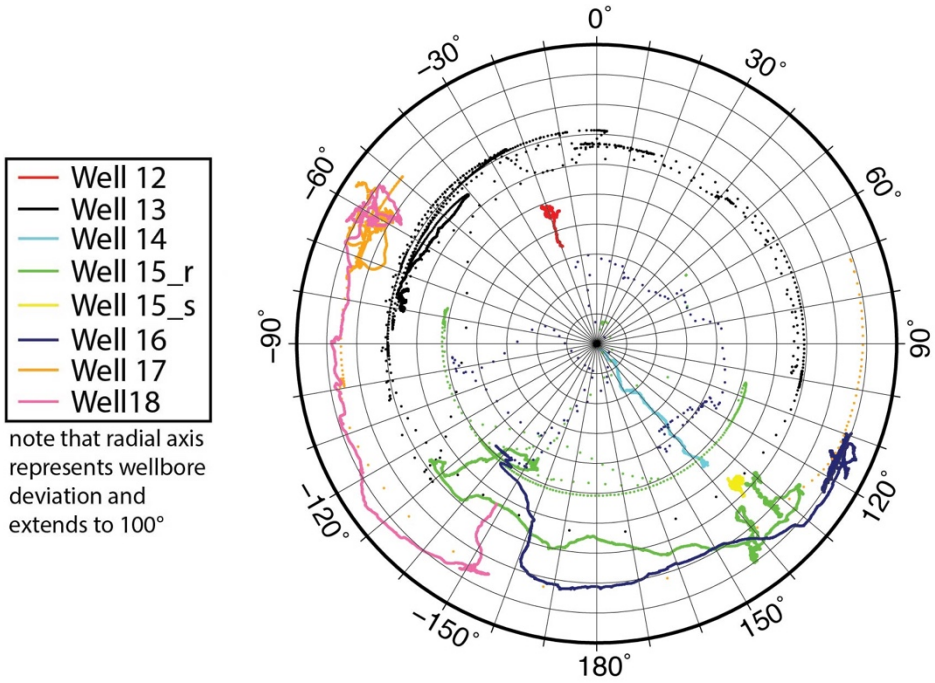

Figure A 10 Polar plot showing all borehole orientations at which 4-arm caliper data were logged at platform Gail. Data points are colored by individual well.

A11. Platform Holly data coverage

We analyzed 11 deviated wells from platform Holly where recorded depths ranged from 545 – 1590 m TVD.). Depths of recorded 4-arm caliper data are shown in Figure A11, and all borehole orientations at which data were logged are shown in Figure A12.

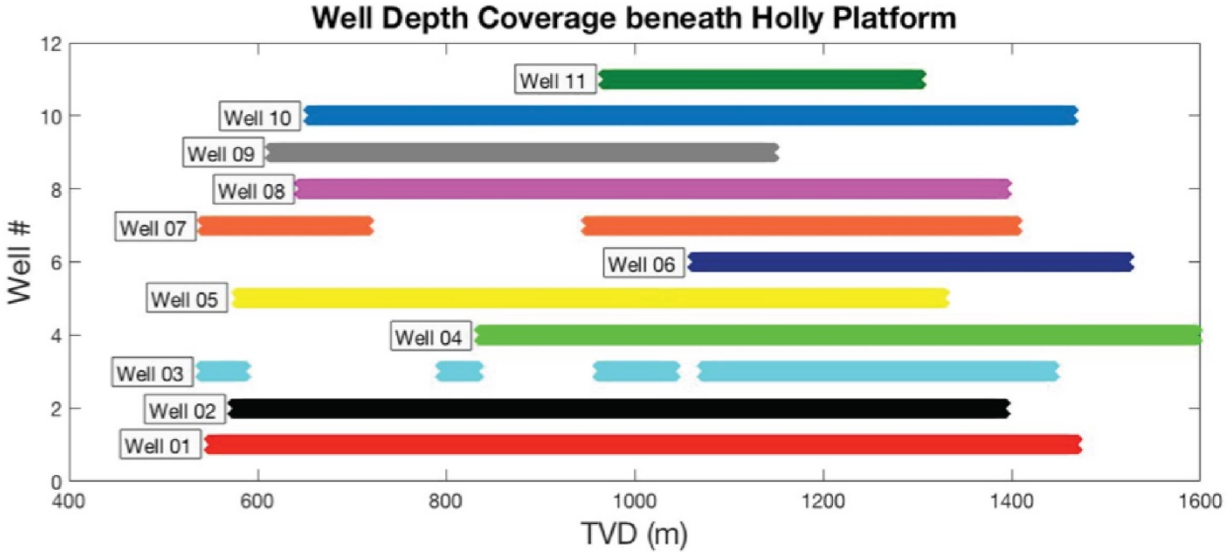

Figure A 12. Graph of borehole depths (TVD - m) at which 4-arm caliper data were logged at platform Holly.

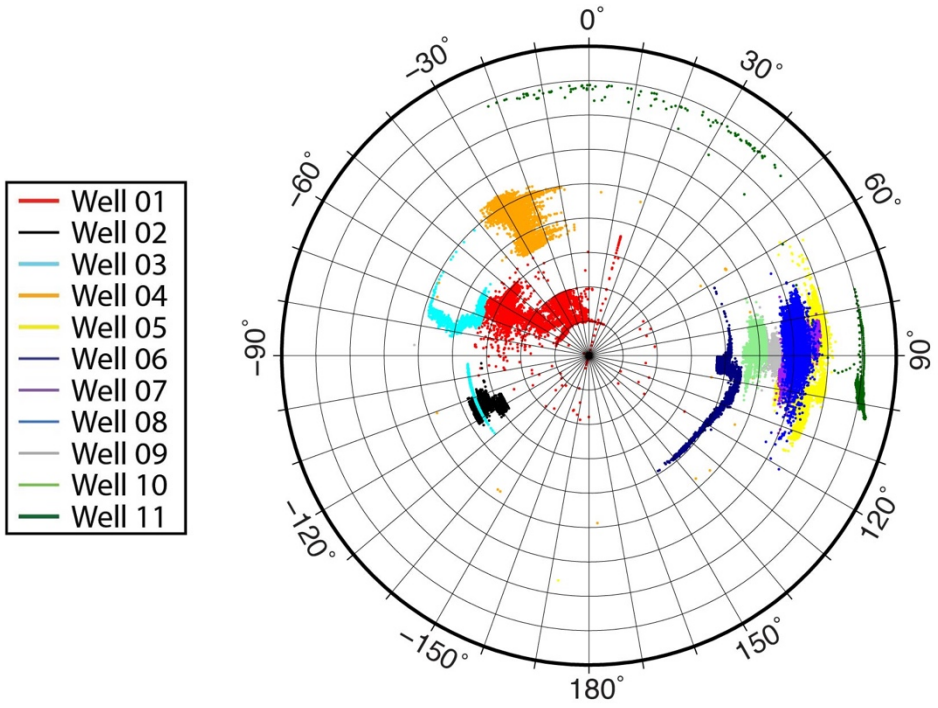

Figure A 11. Polar plot showing all borehole orientations at which 4-arm caliper data were logged at platform Holly. Data points are colored by individual well.

A12. Breakout width from 4-arm caliper data

We have identified wellbore sections where caliper lengths indicate the presence of a borehole breakout, but tool rotation is not obstructed, and instead varies back and forth continuously between two clear extrema, which we believe may represent the edges of a wide breakout (Figure A13). In these cases, our borehole breakout criterion record separate breakout zones at the rotational extrema where tool rotation changes directions, but not between these extrema where the tool rotates freely between the breakout edges. We note that the range of rotation between the two breakout edges could allow for estimation of breakout width, which when combined with estimates of rock strength, can be used to obtain an estimate of the absolute magnitude of S_{Hmax}, a valuable parameter in the quantitative assessment of fault slip potential (Vernik and Zoback, 1992).

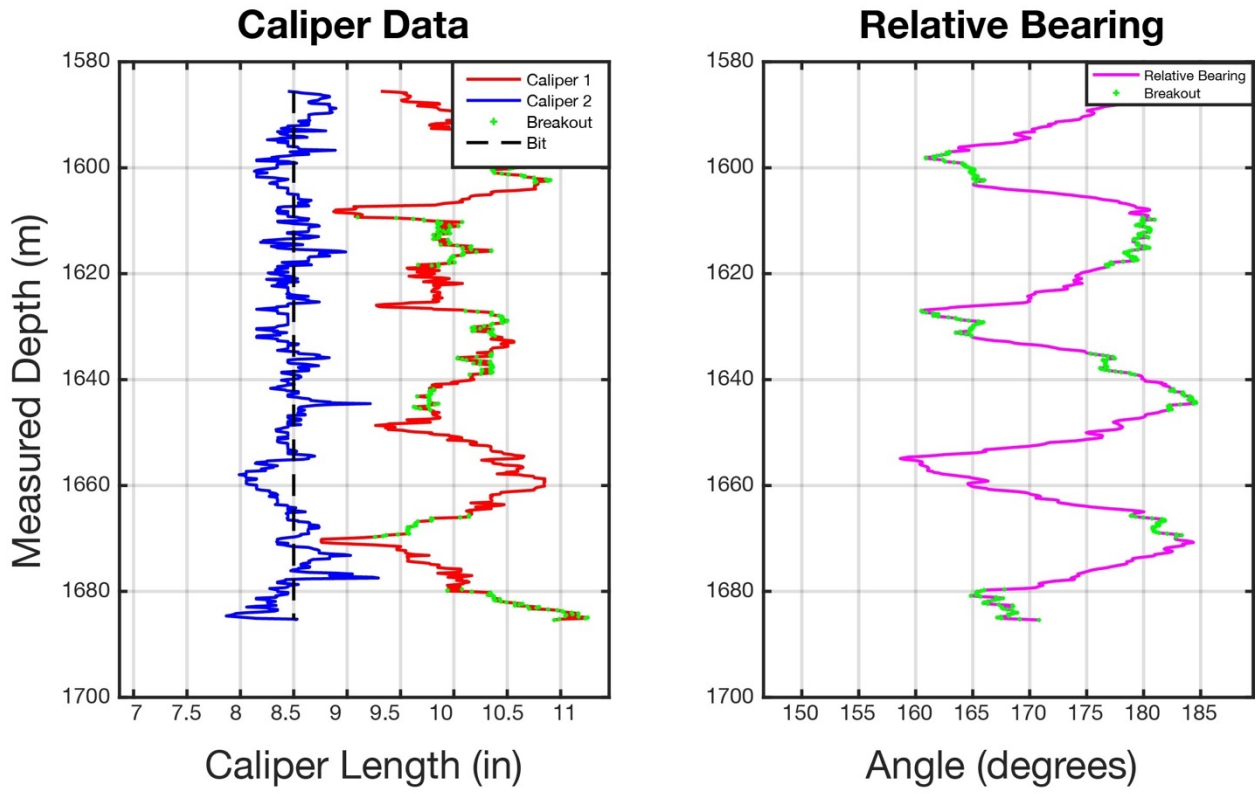

Figure A 13 Caliper (C1 and C2) and Relative Bearing (RB) from a 200 m section of Well 13 from platform Holly where 4-arm caliper log data may allow for estimation of breakout width. Caliper logs meet borehole breakout criteria, but RB varies back and forth between two clear extrema, which we believe may represent the edges of a wide breakout.

A13. Azimuthal range of radial breakouts by aphi (A_ϕ)

All theoretical plots for stress regimes with A_ϕ between 0 - 2.0 have a range of borehole azimuths at which breakouts are expected to form radially (top and bottom of borehole). The width of this azimuthal range decreases from $A_\phi = 0$, where all breakouts are expected to form radially regardless of hole azimuth or deviation, to $A_\phi = 2.0$, where breakouts form radially regardless of deviation at only a single orientation, and rotate away quickly as borehole azimuth changes. Thus, at platform Holly, where 79 of the 89 breakouts identified occurred radially in wellbores that were drilled at an azimuth between N81°E and N99°E, a large range of stress regimes with A_ϕ between 0 - 2.0 exhibit relatively low misfit values at a wide range of S_{Hmax} orientations, resulting in poor constraint of the best fit stress regime and S_{Hmax} orientation.

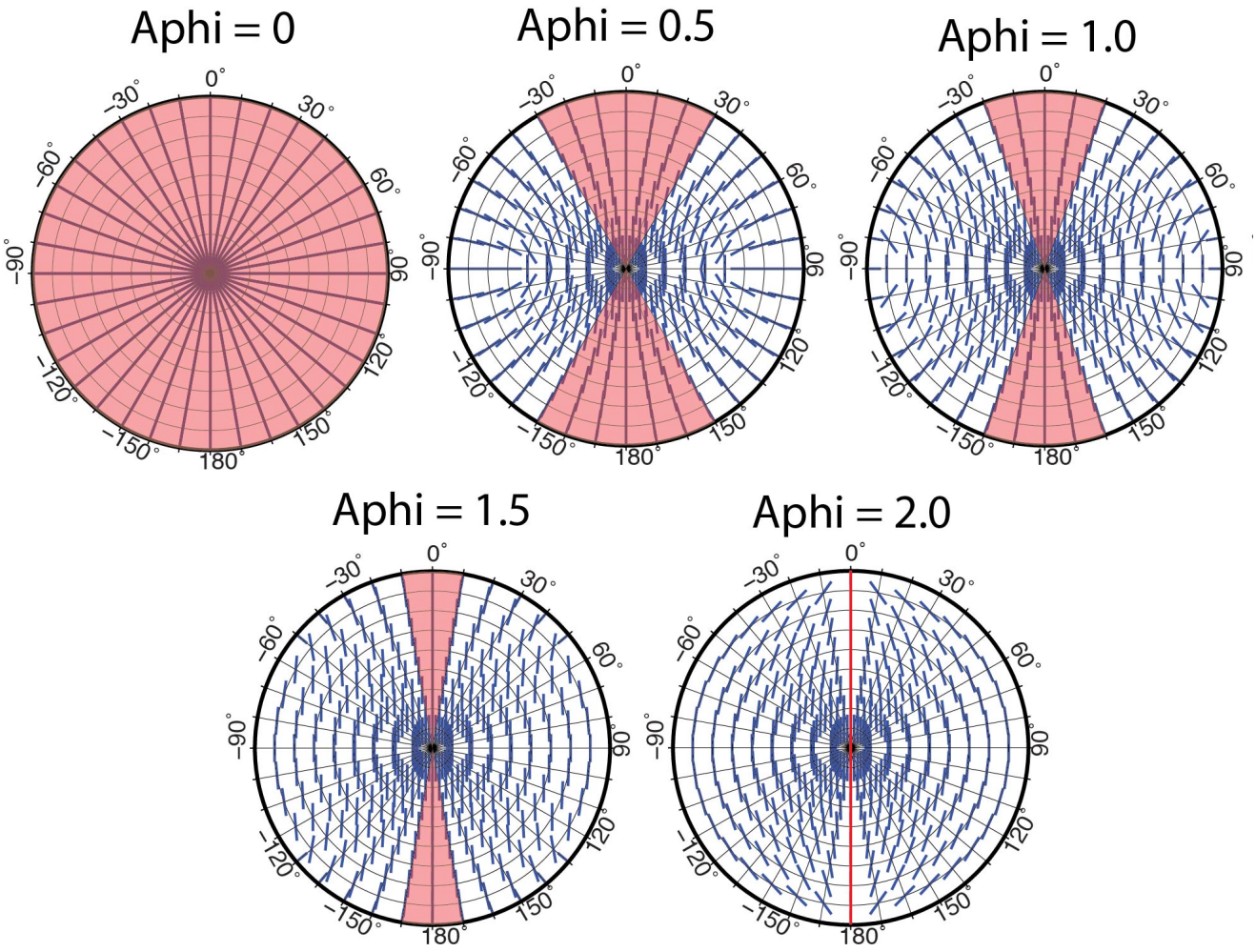

Figure A 14. Theoretical breakout plots for stress regimes with A_ϕ between 0 - 2.0 with the azimuthal range at which breakouts are expected to form radially regardless of borehole deviation highlighted in red. The azimuthal range decreases from $A_\phi = 0$, where breakouts are expected to form radially at all orientations, to $A_\phi = 2.0$, where where breakouts form radially regardless of deviation at only a single orientation, and rotate away quickly as borehole azimuth changes.

A14. Wilde and Stock platform Holly breakouts

Wilde and Stock (1997) identified mostly radial borehole breakouts in wells from platform Holly that were not included in our analysis. These breakouts were identified at borehole azimuths from N90°E to N120°E, from N30°W to N70°W, and from N90°W to N110°W, and support the presence of a thrust faulting regime with A_ϕ between 0-1.0.

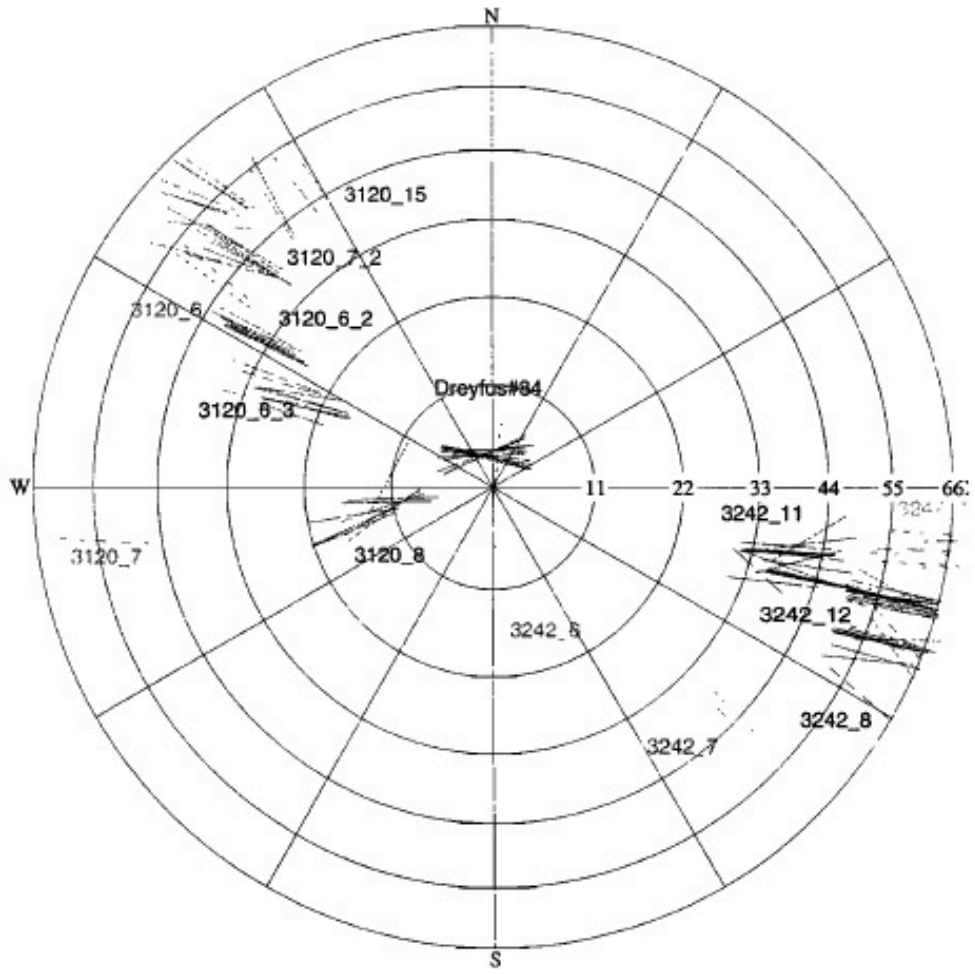

Figure A 15. Lower hemisphere stereographic projection of borehole elongation orientations from boreholes studied in the Santa Barbara region by Wilde and Stock (1997). 3120 and 3242 wells are drilled from platform Holly, and the Dreyfus #84 well is located 20 km north of platform Holly. Wilde and Stock (1997) identified radial breakout orientations in platform Holly wells that were not included in our analysis. These breakouts further support the presence of a thrust faulting stress regime with A_ϕ between 0 - 1.0.

VITA

Edward Harris Pritchard was born in Birmingham, Alabama, but lived the majority of his life in Houston, Texas. As the son of a geologist, his interest in the sciences began at a young age, but he did not take his first Geology course until he was a freshmen at Washington and Lee University. Harris quickly took an interest in the subject, and received his B.S. degree in Geology from W&L in 2016. His undergraduate advisor at the time, Chris Connors, then guided him along the path towards a master's degree in Geology and Geophysics at Louisiana State University. Upon Completion of his master's degree, he will be searching for a job in the oil and gas industry.